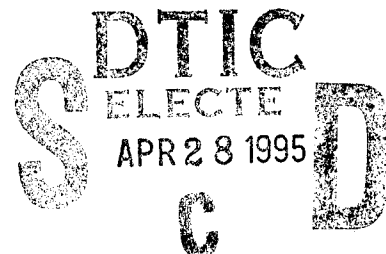# ADAPTIVE OPTICS DESIGN FOR THE ADVANCED ELECTRO-OPTICAL SYSTEM (AEOS)

David W. Tyler
Rockwell Power Systems
PO Box 5670
Albuquerque, NM 87185

Amy E. Prochko
W. J. Schafer Associates, Inc.
2000 Randolph Road, Suite 205
Albuquerque, NM 87106

DTIC
ELECTE
APR 2 8 1995
C

November 1994

Final Report

19950427 128

PHILLIPS LABORATORY
Lasers and Imaging Directorate
AIR FORCE MATERIEL COMMAND
KIRTLAND AIR FORCE BASE, NM 87117-5776

PL–TR—94–1043

This final report was prepared by Rockwell Power Systems, PO Box 5670, Kirtland AFB, New Mexico, under Contract F29601-90-C-0068, Job Order 4241NDAH, with Phillips Laboratory, Kirtland Air Force Base, New Mexico. The Laboratory Project Officer–in–Charge was Dr John Kenemuth (LIMA).
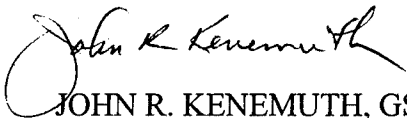
When Government drawings, specifications, or other data are used for any purpose other than in connection with a definitely Government-related procurement, the United States Government incurs no responsibility or any obligation whatsoever. The fact that the Government may have formulated or in any way supplied the said drawings, specifications, or other data, is not to be regarded by implication, or otherwise in any manner construed, as licensing the holder, or any other person or corporation; or as conveying any rights or permission to manufacture, use, or sell any patented invention that may in any way be related thereto.

This report has been reviewed by the Public Affairs Office and is releasable to the National Technical Information Service (NTIS). At NTIS, it will be available to the general public, including foreign nationals.
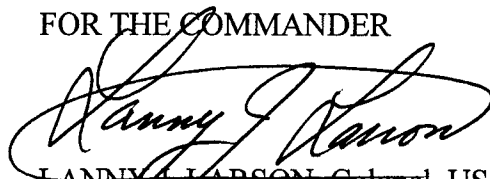
This report has been authored by a contractor of the United States Government. Accordingly, the United States Government retains a nonexclusive royalty-free license to publish or reproduce the material contained herein, or allow others to do so, for the United States Government purposes.

If your address has changed, if you wish to be removed from the mailing list, or if your organization no longer employs the addressee, please notify PL/LIMA, 3550 Aberdeen Ave SE, Kirtland AFB, NM 87117-5776 to help maintain a current mailing list.

This report has been reviewed and is approved for publication.

JOHN R. KENEMUTH, GS-15
Project Officer

JAMES J. McNALLY, Lt Col, USAF
AEOS Program Manager

FOR THE COMMANDER

LANNY J. LARSON, Colonel, USAF
Director, Lasers and Imaging Directorate

DO NOT RETURN COPIES OF THIS REPORT UNLESS CONTRACTUAL OBLIGATIONS OR NOTICE ON A SPECIFIC DOCUMENT REQUIRES THAT IT BE RETURNED.

REPORT DOCUMENTATION PAGE

Form Approved
OMB No. 0704-0188

1. AGENCY USE ONLY *(Leave blank)*	2. REPORT DATE	3. REPORT TYPE AND DATES COVERED
	November 1994	Final Report, Mar 93 – Mar 94

4. TITLE AND SUBTITLE

Adaptive Optics Design for the Advanced Electro-Optical System (AEOS)

5. FUNDING NUMBERS

C: F29601-90-C-0068
PE: 35910F
PR: 4241
TA: ND
WU: AH

6. AUTHOR(S)

David W. Tyler and Amy E. Prochko*

7. PERFORMING ORGANIZATION NAME(S) AND ADDRESS(ES)

Rockwell Power Systems
PO Box 5670
Kirtland AFB NM 87185

8. PERFORMING ORGANIZATION REPORT NUMBER

9. SPONSORING/MONITORING AGENCY NAME(S) AND ADDRESS(ES)

Phillips Laboratory
3550 Aberdeen Avenue
Kirtland AFB NM 87117-5776

10. SPONSORING/MONITORING AGENCY REPORT NUMBER

PL-TR--94-1043

11. SUPPLEMENTARY NOTES

*Amy Prochko is with W.J. Schafer Associates, Inc., 2000 Randolph Road, SE Suite 205, Albuquerque, NM 87106

12a. DISTRIBUTION/AVAILABILITY STATEMENT

Approved for public release; distribution is unlimited

12b. DISTRIBUTION CODE

13. ABSTRACT *(Maximum 200 words)*

We develop an algorithm to guide the use of computer simulations in the design of application-specific adaptive optics (AO) systems. We then use this method to specify the number of deformable-mirror actuators and closed-loop bandwidth for the Advanced Electro-Optical System (AEOS) telescope AO system. To develop the algorithm we present analysis to show the normalized on-axis intensity can be minimized for a given AO configuration by selecting an optimum imaging wavelength. This wavelength minimizes the combined effects of diffraction, which increases with wavelength, and residual (post-compensation) phase aberration, which decreases as wavelength increases. We also show that the closed-loop AO bandwidth minimizing the sum of wavefront sensor noise error and control loop lag error is independent of wavelength. This allows the optimum bandwidth-wavelength combination for any AO configuration to be calculated non-iteratively in two steps. We describe a high-fidelity computer simulation and measures of merit used to select from amoung four candidate configurations. Finally, we present simulation results used to select the AEOS adaptive optics configuration and recommend the AEOS system use approximately 700 actuators with a maximum closed-loop bandwidth of at least 400 Hz.

14. SUBJECT TERMS

Adaptive Optics, Adaptive Optics Design, Advanced Electro-Optical System (AEOS), Atmospheric Compensation, Ground-Based Satellite Imaging

15. NUMBER OF PAGES

64

16. PRICE CODE

17. SECURITY CLASSIFICATION OF REPORT	18. SECURITY CLASSIFICATION OF THIS PAGE	19. SECURITY CLASSIFICATION OF ABSTRACT	20. LIMITATION OF ABSTRACT
Unclassified	Unclassified	Unclassified	SAR

NSN 7540-01-280-5500

Standard Form 298 (Rev. 2-89)
Prescribed by ANSI Std. Z39-18
298-102

ACKNOWLEDGEMENTS

Accesion For		
NTIS CRA&I	☑	
DTIC TAB	☐	
Unannounced	☐	
Justification		
By		
Distribution /		
Availability Codes		
Dist	Avail and / or Special	
A-1		

Contents

1. __INTRODUCTION__

Adaptive optics (AO) are used in optical systems to compensate for aberrated light in real time [1]. For ground-based telescope applications, atmospheric turbulence can severely degrade resolution for pupil diameters much larger than r_o, the Fried coherence diameter, but the use of adaptive optics can significantly increase image quality. Adaptive optics techniques can allow space objects to be imaged with resolution near the diffraction-limit of the telescope and are the state-of-the-art technology for imaging through the atmosphere.

An adaptive optics system typically consists of a wavefront sensor (WFS), deformable mirror (DM) and a control system, as illustrated [2] in Fig. 1. An atmospherically distorted wavefront enters the telescope and reflects off the DM to a beamsplitter sending light to an imaging camera and a wavefront sensor. The WFS estimates the phase profile over the telescope pupil, and the signals from this measurement are used by the control system to conjugate the pupil phase with the DM [3]. Ideally, the resulting image is then free of turbulence-induced optical effects. Since the WFS observes the DM along with the imaging camera, the signals from the control system to the deformable mirror form a feedback loop.

Current ground-to-space imaging applications utilizing adaptive optics technology include astronomy and satellite/debris imaging, with the Department of Defense (DoD) Advanced Research Projects Agency (ARPA) sponsoring most research. Among the DoD-operated telescopes equipped with adaptive optics systems are the Air Force Maui Optical Station (AMOS) and the Starfire Optical Range (SOR) at the USAF Phillips Laboratory (PL), which are used here as a reference for the progression in technology. Air Force-sponsored gains in imaging capability benefit both military and civil observing programs [4–6].

The Compensated Imaging System (CIS) was designed for the 1.6-m AMOS telescope on Mt. Haleakala, Maui. The CIS has 168 actuators and 152 subapertures [7] and uses a shearing interferometer WFS. This decade-old system operates at a closed-loop bandwidth of 2 kHz and is the "workhorse" for AF Space Command optical data collection. AMOS is
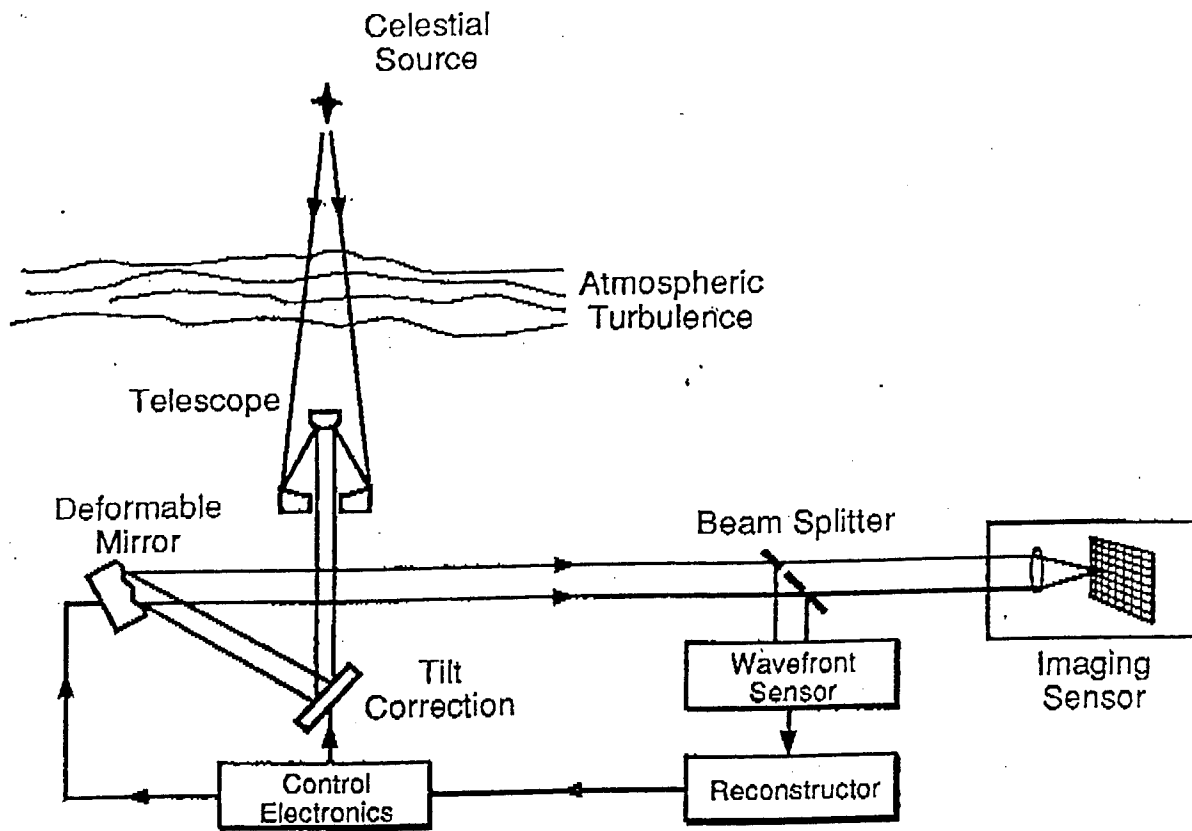
Figure 1: A typical adaptive optics scheme. Reprinted with permission of MIT Lincoln Laboratory, Lexington, Massachusetts.

an operational facility that performs research on an as-available basis.

The Starfire Optical Range is a dedicated research facility at the Phillips Laboratory in Albuquerque, New Mexico. Two generations of adaptive optics have been developed for the 1.5-m telescope at SOR [8]. The First Generation system operates at a 65 Hz closed-loop bandwidth with 150 independent actuators, and the Second Generation system at 130 Hz with 241 independent actuators. Both use continuous facesheet deformable mirrors and Shack-Hartmann wavefront sensors. Researchers at SOR have demonstrated the capability to use adaptive optics with a laser guide star generated by Rayleigh backscatter at 10 km range [9].

The Advanced Electro-Optical System (AEOS) telescope will serve the military, astronomers, and atmospheric scientists. AEOS is a congressionally-directed project and will enhance the capabilities of the AMOS facility. AEOS will be a larger telescope (3.67 m) with a more sophisticated AO system, making possible higher resolution than currently obtainable with the 1.6-m instrument. SOR research over the past twelve years has been incorporated in the design and specification of the AEOS telescope and adaptive optics. A similar AO system will be installed on the new SOR 3.5-m telescope, and continuing SOR research is expected to generate periodic improvements to the AEOS facility. Also, results from research into "hybrid" imaging concepts, or combinations of AO compensation and various statistical post-processing techniques, have been incorporated in the AEOS adaptive optics design. Hybrid imaging was pioneered at the Phillips Laboratory [10] and has been studied extensively during experiments at AMOS [11–13] and SOR [14]. Hybrid techniques are considered "state of the art," and certain post-processing methods have been refined to the point where they are indispensable partners for adaptive optics systems.

The AEOS adaptive optics system was designed using a new approach [15]. Rather than designing a system as complex as technology allows, the system has been customized to meet the needs of the primary user. A step-by-step approach, employing computer simulation, analysis and user input was developed for this project to ensure the AEOS AO system is optimally configured. This method is described in the second section. The third section

contains a description of the simulation, the measures of merit, and the results. Finally, the recommended AEOS adaptive optics system is described.

2. DESIGN METHOD

2.1. AN ALGORITHMIC APPROACH TO ADAPTIVE OPTICS DESIGN

As adaptive optics engineering has become more mature, design of an AO system has evolved from simply choosing the most robust system allowed by technology and budget constraints. Particular emphasis has been placed recently on the differences in AO performance required for astronomical imaging in the near-infrared and DoD missions such as satellite imaging and laser aiming [4]. For example, the motion of stellar objects in a telescope's field of view (FOV) is due only to the rotation of the earth; a satellite's orbital velocity carries it through a given FOV at a considerably higher speed. This requires the AO system to sample the atmosphere at a much higher rate with comensurate demands on the system hardware. These differences in requirements and the associated costs for varying applications call for a move toward customizing the design of an AO system to meet the needs of individual users. We have developed a systematic way of using computer simulations to select the optimal number of DM actuators and WFS subapertures for a given AO system and application, and we have applied the method to the design of the 3.67-meter Advanced Electro-Optical System telescope adaptive optics [15].

The essence of the method can be given by the following two steps:

1 Select several candidate AO configurations, specifying the number of actuators and subapertures for each system to sample the space between the most robust, highest-order system possible and the lowest desirable.

2 Compare the systems in a few stressing but representative scenarios of importance to the user.

In Step One, we assume enough knowledge of the application and telescope to set a lower bound for AO system sophistication; *e.g.*, while image stabilization (tilt-removal) may concievably suffice for astronomical imaging at 2.2 μm on a 1-m telescope, it may not be

worth considering for high-resolution imaging in the visible band on a larger telescope. We also assume enough understanding of AO technology to set an upper performance bound, which may be described in terms of anticipated future developments or the current state of the art. Also implicit in Step One is an understanding of atmospheric and seeing conditions at the site where the proposed system is to be used. This information is necessary to specify the minimum performance required.

Step Two assumes a firm understanding of the telescope user's needs. Implicit in the phrase "stressing but representative scenarios" is test conditions near the upper bound of what might be expected in terms of AO performance for the user's application, requiring a thorough knowledge of expected AO reference brightnesses, telescope slew rates, and the ultimate use of the imagery. A metric appropriate to the application and sensitive enough to show easily recognizeable and interpretable change as parameters are varied is necessary for Step Two, and the metric may have to be developed *ad hoc* from knowledge of the user's needs.

The specific case of the AEOS design illuminates the practical issues in carrying out Step Two. Consider that the closed-loop bandwidth of the AO control system governs two competing effects: As bandwidth is increased, the WFS sampling period is decreased and fewer photons are collected in each subaperture. This causes WFS measurement noise to increase and AO performance to suffer. Conversely, as the bandwidth is decreased, measurement noise decreases, but since the atmospheric aberration being measured is evolving in time, a slower control loop eventually leads to lower AO performance because the system will be attempting to compensate an aberration that no longer exists in the same form. This implies the existence of an optimal bandwidth for an AO system, dependent on WFS reference brightness and the atmospheric time constant. However, AO systems with relatively fewer actuators and subapertures not only collect more photons per wavefront sample because of the larger subaperture pupils, but are less affected by control-loop delay errors [16], implying a different optimum bandwidth for different systems.

The imaging wavelength λ affects AO performance similarly. As λ increases, the severity

6

of the atmospheric aberrations decreases, causing an increase in achievable resolution and reducing the performance required of the AO system. However, diffraction also increases, reducing resolution and implying an optimum imaging wavelength. This optimum wavelength can also be seen to be different for each candidate system by considering limiting cases: For a telescope equipped only with a tilt-removal system, the optimum λ would be long enough that the Fried coherence length r_o is somewhat larger than the telescope pupil, restricting the need for AO to image stabilization. For a telescope with a very large number of actuators in an AO system, the optimum imaging wavelength could be short enough that r_o is half the diameter of the WFS subapertures, assuming a bright enough WFS reference.

To fairly compare adaptive optics systems with different numbers of DM actuators and WFS subapertures, we should calculate the appropriate metric at the optimum control-loop bandwidth and optimum wavelength for each system. Step Two may thus be restated as, "Find the global extremum of a metric on a 'performance surface.'" Such a surface is shown in Figure 2. This gives, for a specified AO configuration, each system's optimum operating wavelength and bandwidth and the associated performance in terms of the metric. Different configurations can then be compared.

Blindly searching the performance surface, however, is in general tedious and time consuming even using a computer simulation. This motivates the use of analytical techniques for an initial operating point solution. This work is outlined in the next section.

2.2. PRELIMINARY ANALYSIS

The results of our preliminary analysis form the basis for actually performing the comparison required by Step Two of the design method. First, a suitable metric must be chosen to find the optimum operating points for the candidate systems. For the purposes of the AEOS study, we found the normalized on-axis intensity I_n to be nearly ideal. We define I_n as the peak intensity normalized to the total:

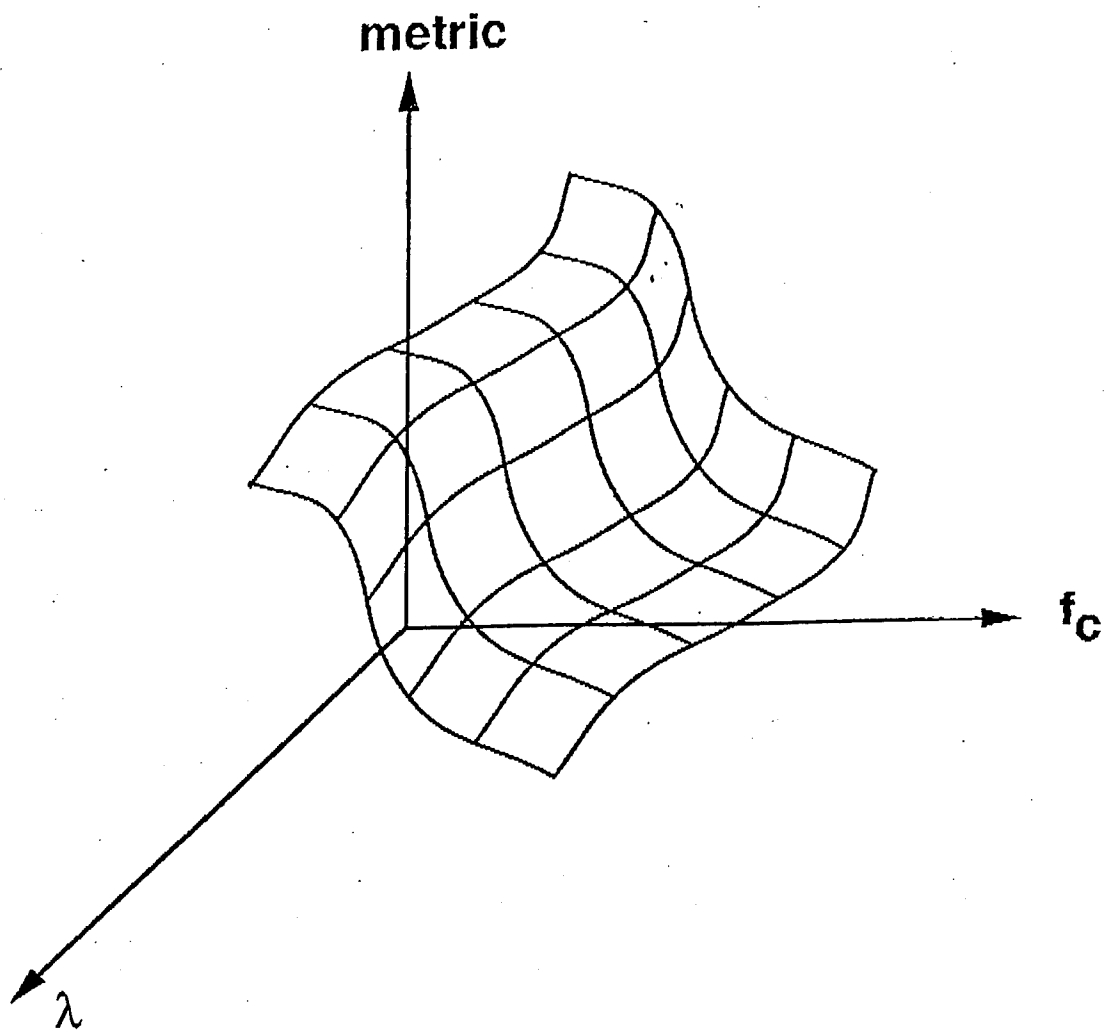$$I_n = \frac{P(\mathbf{r} = 0)}{\int P(\mathbf{r}) d^2\mathbf{r}}, \tag{1}$$

Figure 2: Visualization of the wavelength-bandwidth optimization problem. Coupling between the two variables f_c and λ would make the optimization problem very difficult to solve analytically.

where $P(\mathbf{r})$ is the average point spread function (PSF) and $\mathbf{r}$ is the two-dimensional focal plane spatial coordinate vector. Keeping in mind the definition of Strehl [17] and assuming the average point-spread function resembles an Airy disk, we can multiply S by the peak intensity of an Airy disk and express a quantity I^* proportional to I_n:

$$I^* = (\frac{D}{\lambda})^2 (1 - \sigma_{r,t}^2),\qquad(2)$$

where $\sigma_{r,t}^2$ is the total residual phase variance. Note in writing the peak intensity as $(D/\lambda)^2$, we have set the total intensity subtended by the telescope to unit value. Also, we have used the factor $(1 - \sigma_{r,t}^2)$ to approximate the Strehl ratio for small residual phase variance. The total residual variance may be written as the sum of three independent terms

$$S \approx 1 - (\sigma_{r,N}^2 + \sigma_{r,f_c}^2 + \sigma_{r,SNR_W}^2),\qquad(3)$$

where $\sigma_{r,N}^2, \sigma_{r,f_c}^2$, and σ_{r,SNR_W}^2 are the variances due to fitting error with N deformable mirror actuators, control loop lag error with closed-loop bandwidth f_c, and wavefront sensor measurement error due to signal-to-noise ratio SNR_W, respectively.

Assuming that N actuators will reasonably correct N Zernike terms allows us to use the well-known expression for the mean-square residual phase error from fitting error [18,19] in place of $\sigma_{r,N}^2$:

$$\sigma_{r,N}^2 = 0.3(D/\sqrt{N}r_o)^{5/3},\qquad(4)$$

where D is the pupil diameter. The residual error due to finite bandwidth is given by [20]

$$\sigma_{r,f_c}^2 = (\frac{f_G}{f_c})^{5/3},\qquad(5)$$

where f_G is the Greenwood frequency. The Greenwood frequency f_G is a measure of the bandwidth at which the WFS must sample the atmosphere. The residual error due to wavefront sensor noise can be written approximately by [21]

$$\sigma_{r,SNR_W}^2 \approx (\frac{\pi}{SNR_W})^2 \frac{\pi}{10}.\qquad(6)$$

9

The wavefront sensing error is discussed further in the next section.

To obtain the optimum wavelength λ_o for a system with a given N, f_c, and wavefront sensor SNR, one may assume λ_o gives the sharpest point-pread function or maximum I^* and simply take the derivative of (3) with respect to λ.

To do this, write (4) and (5) in terms of λ and "reference" quantities R_o and F_G which define r_o and f_G for a fixed wavelength. The r_o and f_G quantities are determined by the C_n^2 atmospheric turbulence profile. Choosing the reference wavelength to be .5 μm, for example,

$$r_o = R_o \left(\frac{\lambda}{0.5 \times 10^{-6}} \right)^{6/5}, \tag{7}$$

and

$$f_G = F_G \left(\frac{0.5 \times 10^{-6}}{\lambda} \right)^{6/5}. \tag{8}$$

The choice of the imaging wavelength λ manifests itself in WFS slope-measurement error as a linear scaling with the ratio of λ to the WFS wavelength, so the mean-square error in (6) may be rewritten

$$\sigma_{r,SNR_W}^2 = \left(\frac{\pi}{SNR_W} \right)^2 \frac{\pi}{10} \left(\frac{\lambda_{WFS}}{\lambda} \right)^2. \tag{9}$$

Using (4)-(9) in (3) reveals that the variance in (2) goes as $1/\lambda^2$, allowing one to rewrite (2) as

$$I^* = \frac{K_1}{\lambda^2} \left(1 - \frac{K_2}{\lambda^2} \right), \tag{10}$$

where $K_1 = D^2$ and

$$K_2 = (0.5 \times 10^{-6})^2 \left[0.3(D/\sqrt{N}R_o)^{5/3} + \left(\frac{F_G}{f_c} \right)^{5/3} \right] + \left(\frac{\pi \lambda_{WFS}}{SNR_W} \right)^2 \frac{\pi}{10} \tag{11}$$

This allows us to take the derivative mentioned earlier and find

$$\lambda_o = \sqrt{2K_2}. \tag{12}$$

The limits of this work are made apparent by the fact that (10) has a zero where $\sigma_{r,t}^2$ times the ratio $(.5 \times 10^{-6}/\lambda)^2 = 1$. This occurs because the expression $S \approx 1 - \sigma_{r,t}^2$ is only

valid for small $\sigma_{r,t}^2$. In Figures 3-6, we compare simulation results at various atmospheric transmission bands and evaluation of (10) over a matching range of wavelengths. In general, the simulation peaks are somewhat broader than those predicted by analysis, with the simulation I_n values diverging away from those given by (10) away from the maximum. Since the maximum Strehl ratio for the simulation runs in these figures is 0.83 and the mean Strehl only 0.52, the approximation for Strehl used to derive (10) is weak, and one should not expect extremely good correspondence between the curves. However, the concern here is the agreement between location of the peak values, which is good over a variety of seeing conditions and for a variety of AO configurations, as seen in the figures. One may conclude that while (10) must be used with care, (12) is a fairly robust predictor for λ_o.

The optimum closed-loop control bandwidth f_{co} for a given AO geometry can also be found by defining the optimum frequency as that which minimizes the residual phase variance represented by the sum

$$\sigma_{r,f_c}^2 + \sigma_{r,SNR_W}^2. \tag{13}$$

Both terms in the above sum are functions of f_c. For a shot-noise limited WFS detector, SNR_W can easily be written in terms of f_c:

$$SNR_W^2 = (\frac{\phi}{10f_c}), \tag{14}$$

where ϕ is the number of photo-detection events (PDEs) per sec and we assume DM voltages are updated using an average of 10 WFS measurements for control-loop stability. This yields $1/10f_c$ as the integration time of the wavefront sensor. Using (14) in (6) with (5) to form (13), the mimimum variance is seen to occur where f_c is chosen so that

$$\frac{d}{df_c}\sigma^2 = 0 = f_G^{5/3}(-\frac{5}{3}f_c^{-8/3}) + \Lambda^2\frac{\pi^3}{\phi} \tag{15}$$

where Λ is the normalized wavelength λ_{WFS}/λ. Simplifying, the optimum bandwidth f_{co} is given by

$$f_{co} = \left(\frac{\frac{5}{3}f_G^{5/3}\phi}{\pi^3\Lambda^2}\right)^{3/8} \approx 0.33\, f_G^{5/8}\left(\frac{\phi}{\Lambda^2}\right)^{3/8} \tag{16}$$

11

Figure 3: Correspondence between simulation I_n vs. λ and predicted on-axis intensity curve for a 741-actuator system with $r_o = 18\ cm$ at $\lambda = 0.8\ \mu m$.

Figure 4: Correspondence between simulation I_n vs. λ and predicted on-axis intensity curve for a 741-actuator system with $r_o = 7.5\ cm$ at $\lambda = 0.8\ \mu m$.

Figure 5: Correspondence between simulation I_n vs. λ and predicted on-axis intensity curve for a 325-actuator system with $r_o = 18\ cm$ at $\lambda = 0.8\ \mu m$.
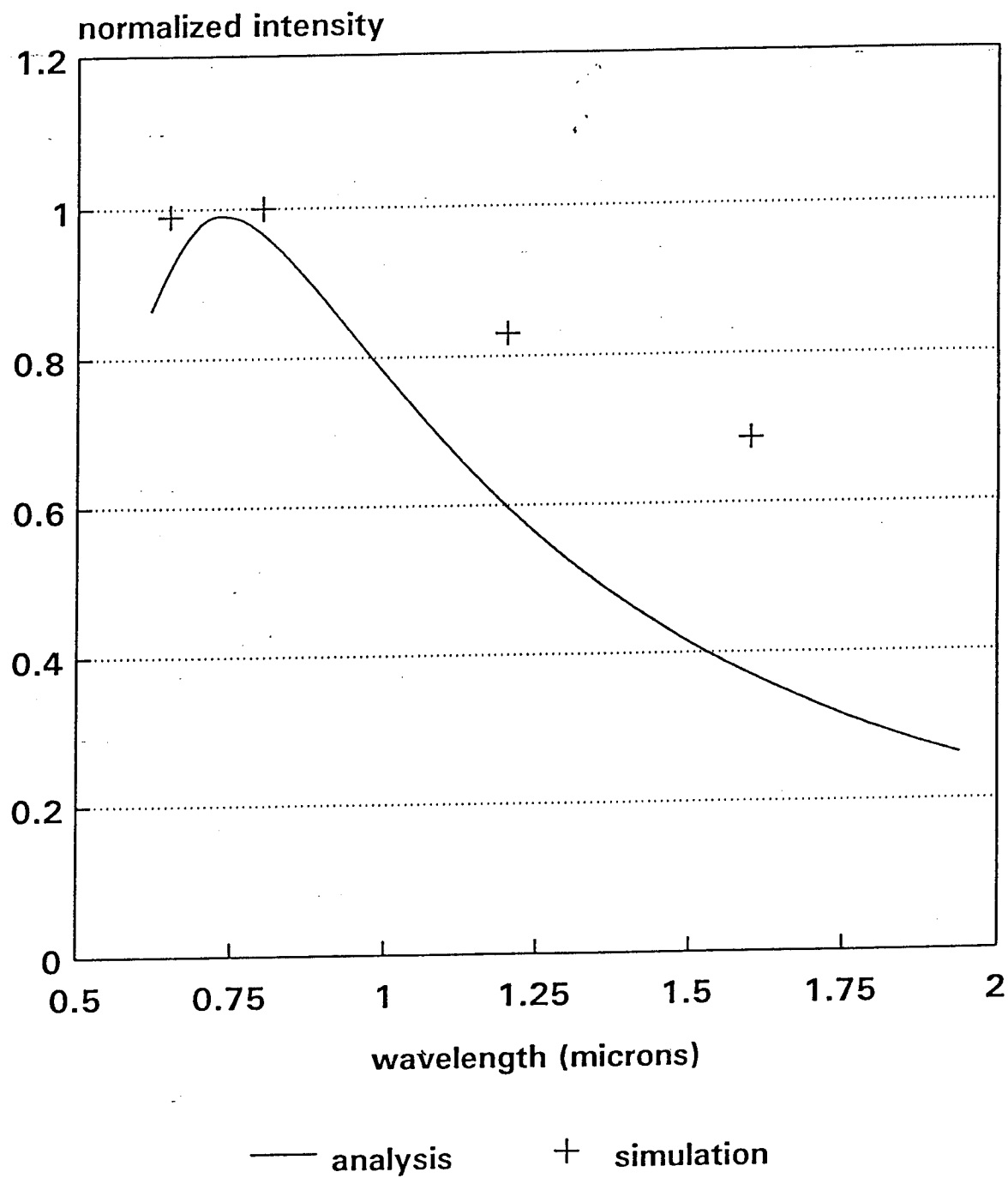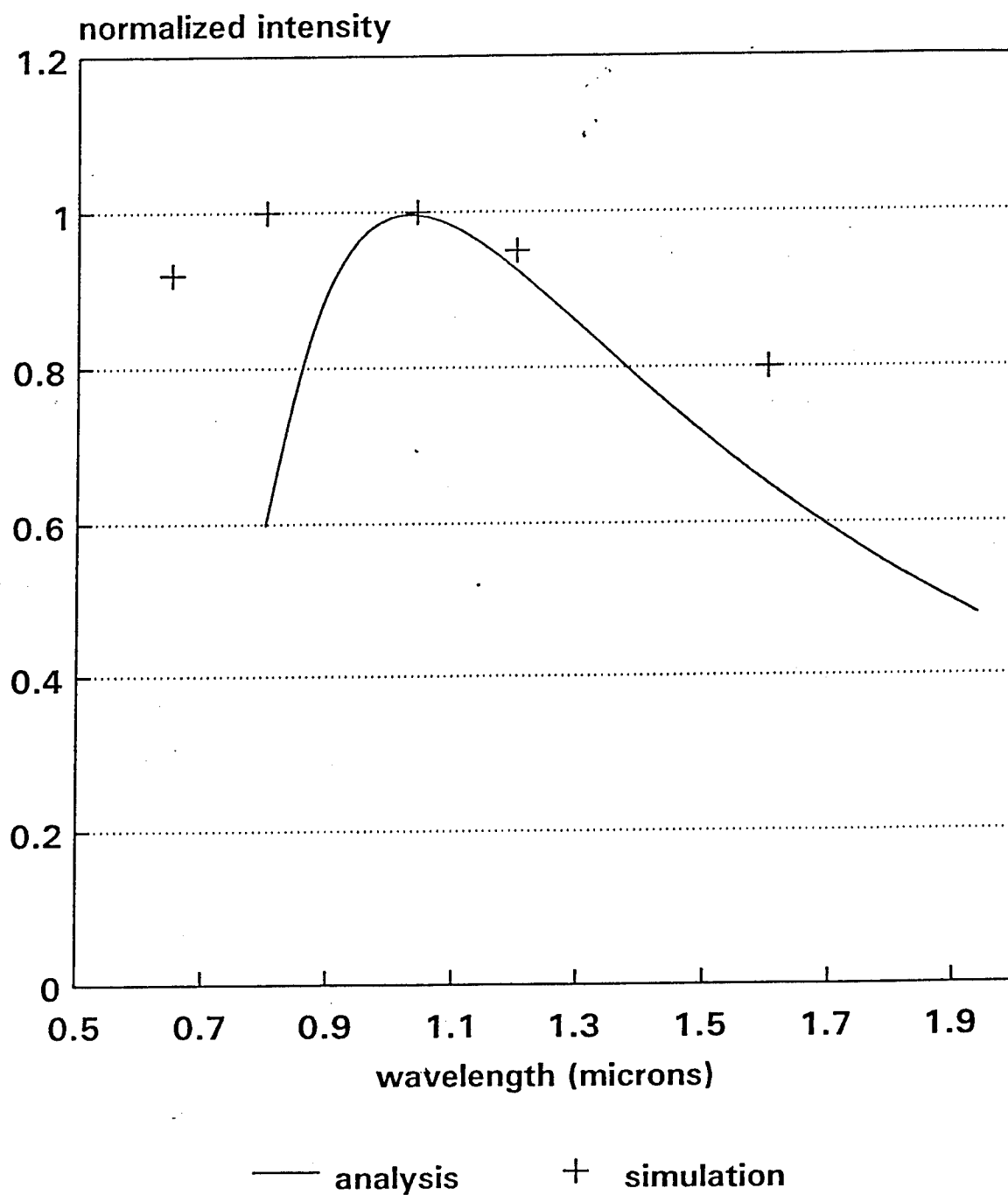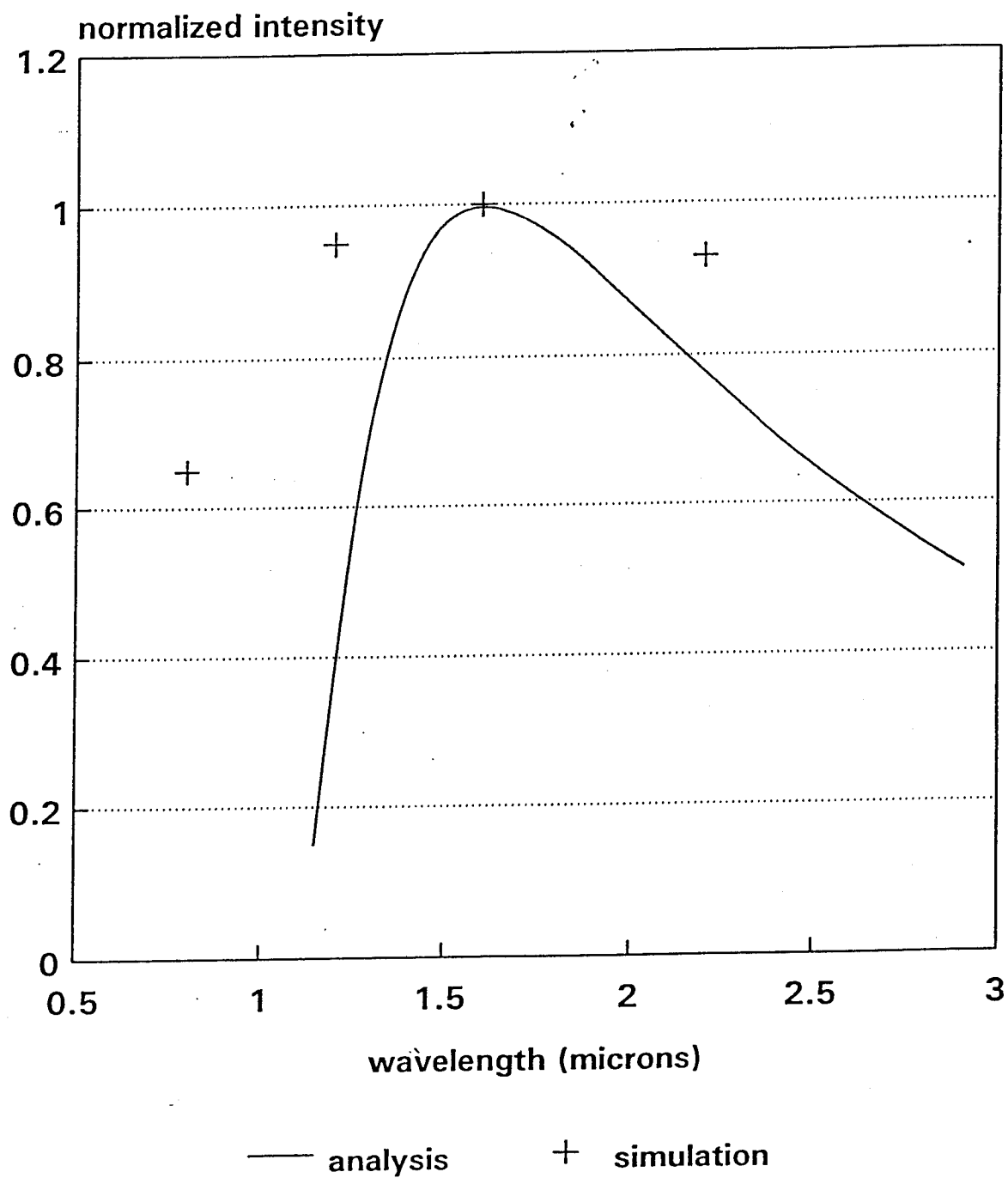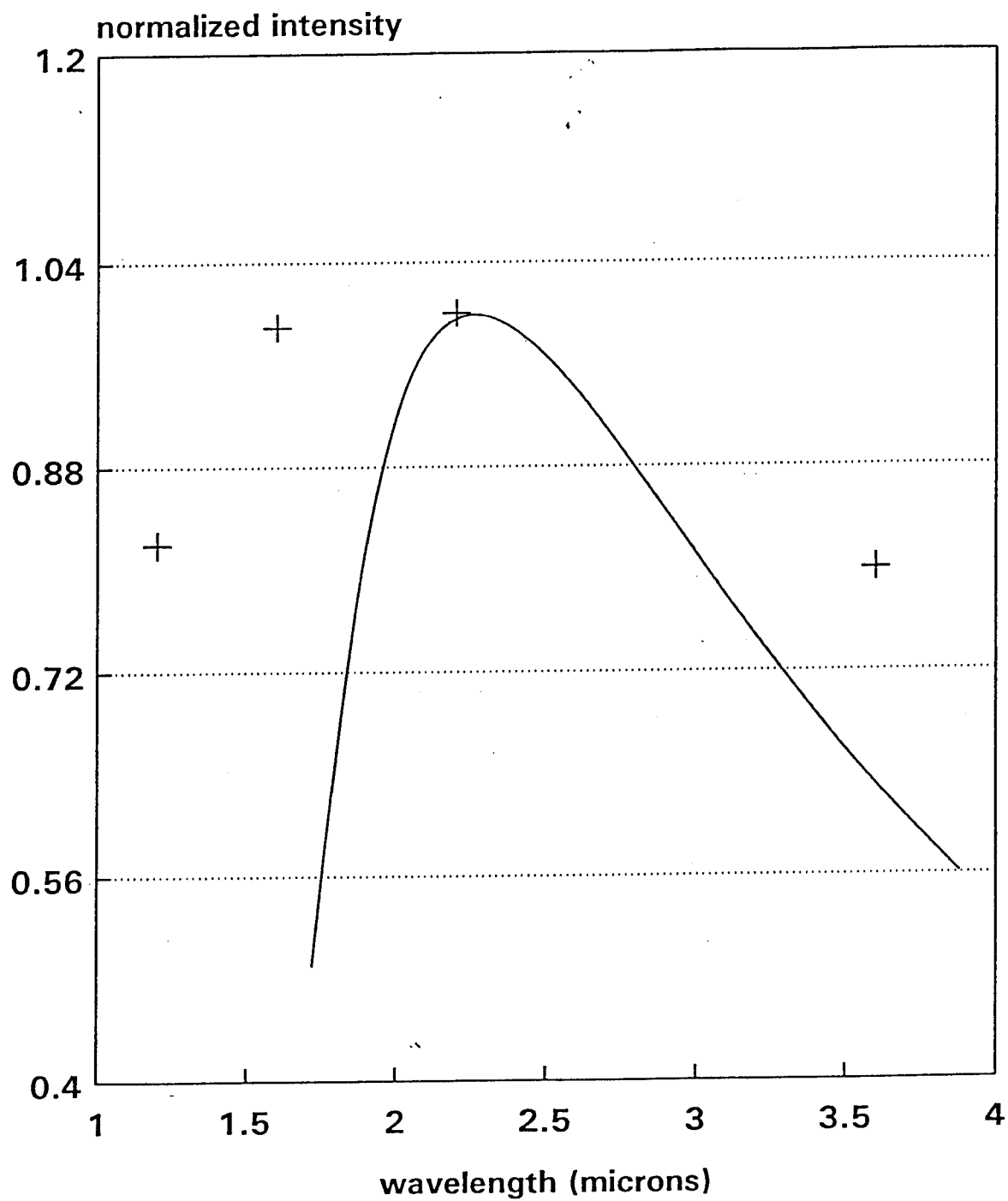
Figure 6: Correspondence between simulation I_n vs. λ and predicted on-axis intensity curve for a 325-actuator system with $r_o = 7.5\ cm$ at $\lambda = 0.8\ \mu m$.

The real utility of this result becomes apparent by using (8) in (16) to write

$$f_G^{5/8} \propto \lambda^{-3/4}. \tag{17}$$

Thus, using the definition of Λ, f_{co} is seen to be functionally independent of the imaging wavelength λ. The results of computer simulations validating (17) are shown in Fig. 7. In this figure, the optimum (minimum σ^2) bandwidth is seen to be independent of imaging wavelength. The independance of f_{co} from λ holds where the WFS and imaging wavelengths are not separated by so much that atmospheric dispersion effects become apparent. The decoupling of the optimum bandwidth and wavelength means that finding an operating point for a given AO configuration can be done in two steps:

1 Calculate the bandwidth giving the minimum mean-square variance (13).

2 Use this f_{co} to calculate the optimum imaging wavelength λ_o.

If f_{co} were a function of λ, the above two steps could be accompished in an iterative series.

Since the variances (4), (5), and (6) are approximate, a detailed computer simulation rather than the above analysis should be considered to calculate the AO operating points. Also, as previously discussed, the expression for I^*, (10), becomes less accurate as seeing degrades, which may further limit the domain in which the analytical method above may be used instead of simulation to find λ_o. Finally, for satellite imaging missions, imaging detector noise effects not accounted for in the derivation of (12) must be considered. For astronomical imaging, the imaging detector can be exposed long enough to mitigate the noise differences between silicon detectors used below $\lambda = 1 \ \mu m$ and materials such as indium gallium-arsenide phosphate (InGaAsP) used for imaging between 1 and 5 μm. Exposure times for satellite imaging, however, are limited by the satellites motion in the telescope FOV as the satellite orbits the earth. If λ_o is calculated from (12) and determined to be beyond 1 μm, computer simulation or a more rigorous analysis must be done to determine whether the increased detector noise decreases I_n more than using a shorter wavelength. However, the preceding work has shown that a suitable metric, I_n, can indeed be maximized

16

ms residual phase at various bandwidths for .8 and 1.2 microns

ms error (radians sqd)

closed-loop bandwidth (Hz)

— ■ — 1.2 microns   —+— 0.8 microns
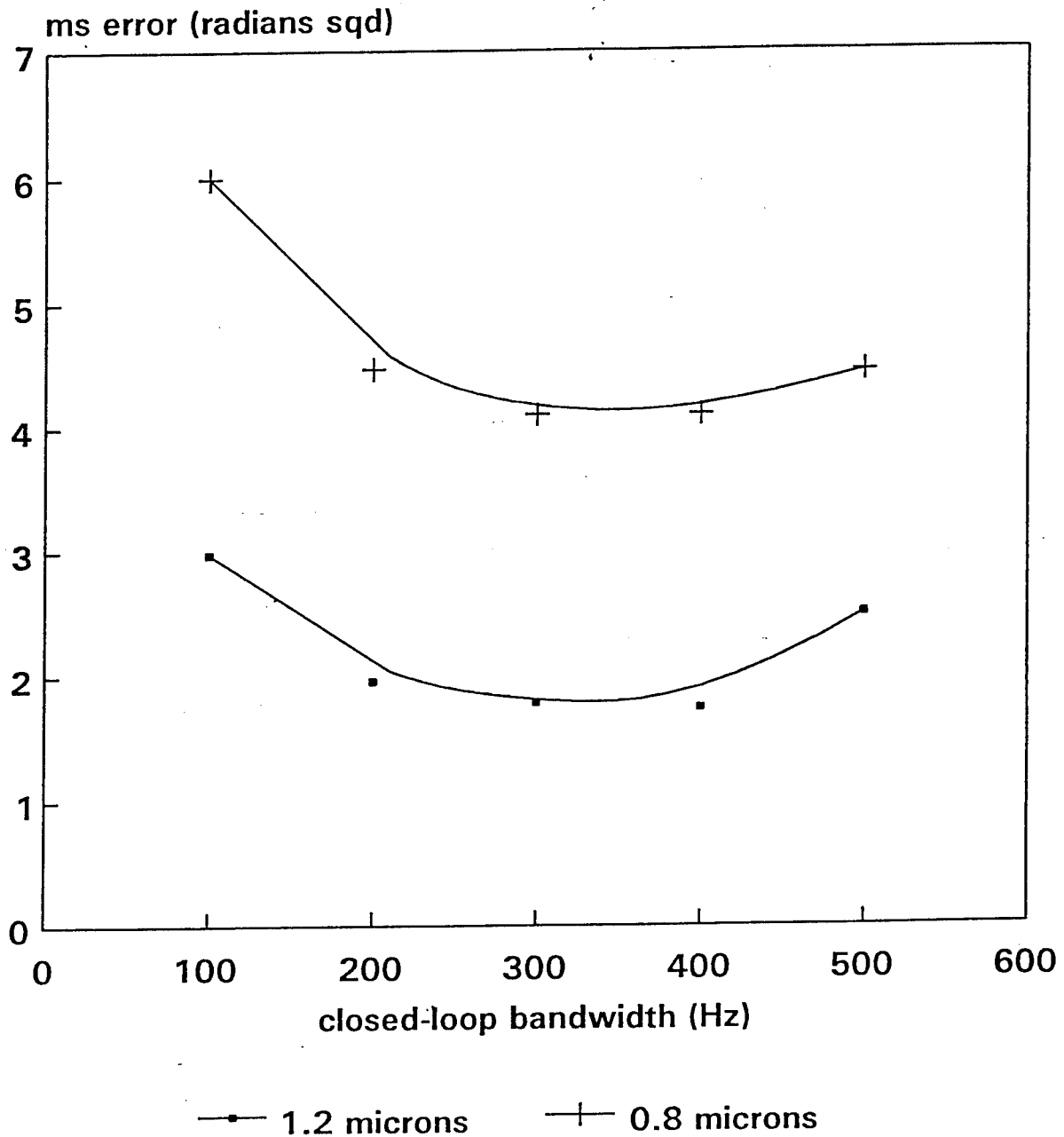
741 actuator system

Figure 7: Mean-square residual phase error vs. bandwidth for $\lambda = 0.8~\mu m$ and $1.2~\mu m$.

by proper choice of imaging wavelength, and that the optimum bandwidth is independent of λ, greatly reducing the computational effort required to locate an operating point for a given AO configuration.

One final caveat concerning implementation of the general method should be pointed out here: We have used approximate analysis to reduce the level of effort required to execute Step Two in the design method for the specific case of the AEOS design. While the approach given in Step One and Step Two provides a general approach for selecting an adaptive optics configuration appropriate for a given application, the analysis in this section, including the use of I_n as a metric, may *not* be appropriate for all applications. For an application where a large FOV is desired, for example, maximum resolution (maximum I_n) may not be desirable, since systems with relatively fewer actuators tend to be less sensitive to anisoplanatism, as well as bandwidth errors [16]. Also, for a particular application, there may be a better definition for the optimum bandwidth f_{co} than that which minimizes the sum of variances given in (13). However, for the AEOS system or any other maximum resolution application, the approach presented here is appropriate.

2.3. COMPARISON SCENARIO

Designing a small number of comparison scenarios that adequately represent the conditions under which the AO system can be expected to perform can be difficult and may indeed be impossible for certain applications. The AEOS mission, though multifaceted, is primarily military surveillance of orbiting satellites, including satellite object identification, mission payload assessment, and operational status assessment (OSA). With the possible exception of OSA, where, for example, an operating satellite power plant may be detected by thermal-infrared photon flux alone, these missions dictate high resolution and relatively short wavelengths.

Also, recent Phillips Laboratory advances in daylight imaging notwithstanding, satellite imaging is only accomplished routinely in "terminator" conditions near sunset or dawn,

where the satellite is illuminated by the sun but the observatory sky is still dark. Since the satellite may not pass near the observatory zenith during terminator hours on any given date, this implies the requirement for high resolution at large zenith angles if the telescope is to deliver imagery in a timely manner. In Table 1, we show the fraction of all low-Earth-orbit (LEO) satellite passes above the observatory horizon in a simulated six-month period that are also higher in the sky than 70, 45, and 20 degree zenith angles; note that the number of observations increases by nearly an order of magnitude from 20 to 70 degrees. Taking these results as a histogram, the probability of a satellite pass near zenith on any given day is actually relatively low. Therefore, timely response to a satellite tasking requires the ability to observe at large zenith angles.

As the zenith angle for a satellite observation increases, signal loss, decreasing r_o, and changing Greenwood frequency impact AO performance. Signal to the AO wavefront sensor and the imaging camera is reduced due to two factors: First, the length of the path taken through the atmosphere by light from the satellite increases, increasing loss to scattering. Second, the increased satellite range means the telescope subtends a smaller solid angle with respect to the satellite, reducing the amount of reflected light from the satellite that is collected by the telescope. The Fried parameter r_o is a function of the inverse of the integrated turbulence, which increases with zenith angle due again to the increase in the thickness of the atmosphere between the satellite and observatory. These first two changes, signal loss and decreased seeing, place a larger burden on the AO system as the zenith angle is increased. However, the Greenwood frequency is affected by two competing phenomena. The increased atmospheric path taken by light from the satellite increases f_G, which increases *with* the integrated turbulence instead of its inverse. At the same time, the angular speed of the satellite relative to the observatory decreases because of increased range, and this decreases f_G by decreasing the telescope tracking slew rate.

If more satellites can be observed more often at high zenith angles *and* the seeing in terms of both r_o and f_G is worse, then a few "stressing but representative" scenarios can be conceived for satellite imaging; all comparisons would be done at relatively high zenith

angles. Therefore, it remains only to calculate which effect, decreased telescope slew or increased atmospheric path, dominates the value of f_G. If the Greenwood frequency is higher at high zenith angles, then high zenith angles are without question both more demanding of the adaptive optics and of more importance to the mission. If f_G is lower at high zenith angles than near zenith, but the Fried parameter is smaller, then further analysis is required to find out whether high or low angles are more demanding.

In fact, the functional dependence of f_G on zenith angle is such that the Greenwood frequency is higher at higher zenith angles. To see this, consider the *isoplanatic angle θ_o* which defines the allowable angular mismatch between the observer-object line of sight and the atmospheric path sampled by the wavefront. It is expressed mathematically by [22]

$$\theta_o^{-1} = [2.91k^2 \int_0^L z^{5/3} C_n^2(z) dz]^{3/5}, \tag{18}$$

where k is the wavenumber $2\pi/\lambda$ and the integral limits are defined by a path of length L through the atmosphere from the observatory to the satellite.

The Greenwood frequency f_G has a very similar definition [20]:

$$f_G = [0.102k^2 \int_0^L v^{5/3} C_n^2(z) dz]^{3/5}, \tag{19}$$

where $v(z)$ is the relative tangential velocity of the airmass between the observatory and the satellite. This relative motion could be due to wind or telescope slew as the satellite is tracked. For most LEO satellite tracking, in fact, v will be predominantly due to slew. This allows us to write f_G in terms of the slew rate Ω:

$$f_G \propto \frac{\Omega}{\theta_o}. \tag{20}$$

Now one may evaluate the Greenwood frequency in terms of the zenith angle ϕ. At culmination, the satellite is at its point of closest approach to the observatory, so the satellite velocity $\mathbf{v}$ is normal to the observatory line of sight. At culmination, then,

$$\Omega = \frac{v}{R} = \frac{v \cos\phi}{A}, \tag{21}$$

where $v = |\mathbf{v}|$, R is the range from the observatory to the satellite, and A is the satellite orbital altitude at culmination. Using (21) in (20),

$$f_G \propto \frac{cos\phi}{\theta_o}. \tag{22}$$

Finally, considering the z-weighting in the integral of (18),

$$f_G \propto (cos\phi)^{-3/5}. \tag{23}$$

As ϕ increases from zero, then, f_G will increase, although the magnitude of the increase will depend on the C_n^2 function.

Since a high zenith-angle engagement is both the most demanding of the adaptive optics and the most likely to allow imaging of a given satellite, a few high-zenith-angle comparison scenarios will be sufficient. The scenarios should specify a dim enough object and large enough zenith angle that WFS noise and bandwidth effects will be apparent in simulations; also, the zenith angle should be large enough to observe wavefront sampling errors due to r_o being smaller than WFS subapertures.

To meet these requirements, we initially chose a comparison scenario using a point-source object at 70 degrees zenith angle, 1200 km range, and visual magnitude 5.9 with a slew rate of 0.8 deg/sec. The object brightness was calculated using sophisticated, three-dimensional satellite models and proven atmospheric and radiometric codes. At this zenith angle, the Fried parameter r_o is about half its value at zenith. Using the Beland night turbulence model for the AMOS site [23], an imaging wavelength of 0.8 μm and a slew rate of 0.9 deg/sec give $r_o = 7.5$ cm and a Greenwood frequency of nearly 500 Hz. While this zenith angle is perhaps atypical of satellite imaging engagements, simulations of different systems at the outer limits of what is realistic unambiguously reveal the vulnerabilities of different configurations, as will be discussed later. However, this scenario caused all candidate systems to have optimal imaging wavelengths beyond 1 μm, which is not a desireable operating point due to relatively higher detector noise in sensors optimized for the 1-5 μm band. This consideration motivated a comparison of the candidate systems at 45 degrees zenith with $\lambda = 0.8$ μm, as well. Under

these conditions, the zenith angle is more representative of a typical engagement although not nearly as demanding of the adaptive optics. Finally, we compared the systems at 70 degrees zenith and 0.8 μm, the most severe conditions.

Figures 8 and 9 show r_o and f_G as a function of zenith angle for 0.8, 1.2, and 1.6 μm.

Fried coherence length for
Beland night turbulence model

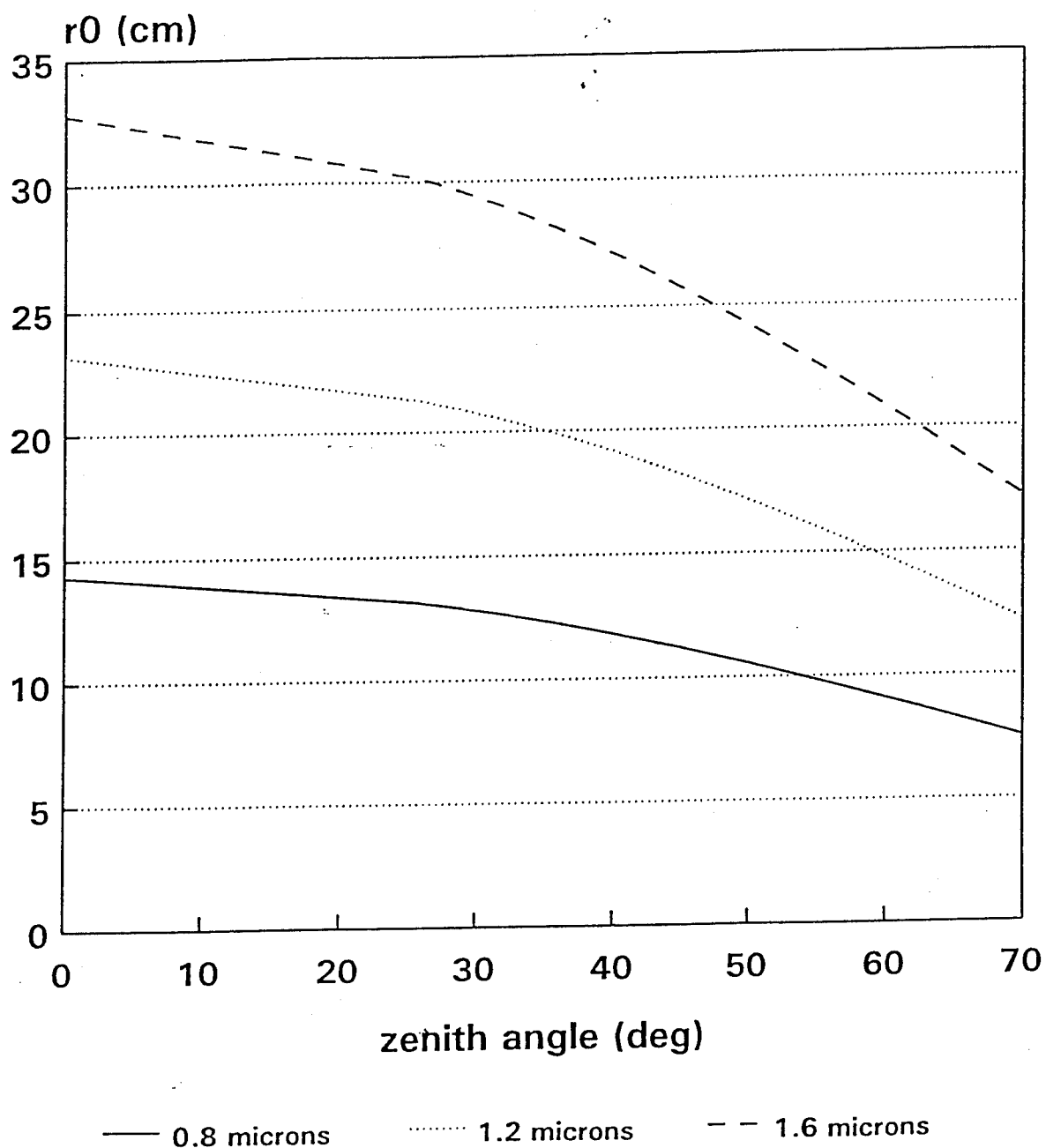Figure 8: Fried coherence diameter r_o vs. zenith angle for Beland night turbulence model at $\lambda = 0.8$, 1.2, and 1.6 μm.

Greenwood frequency for
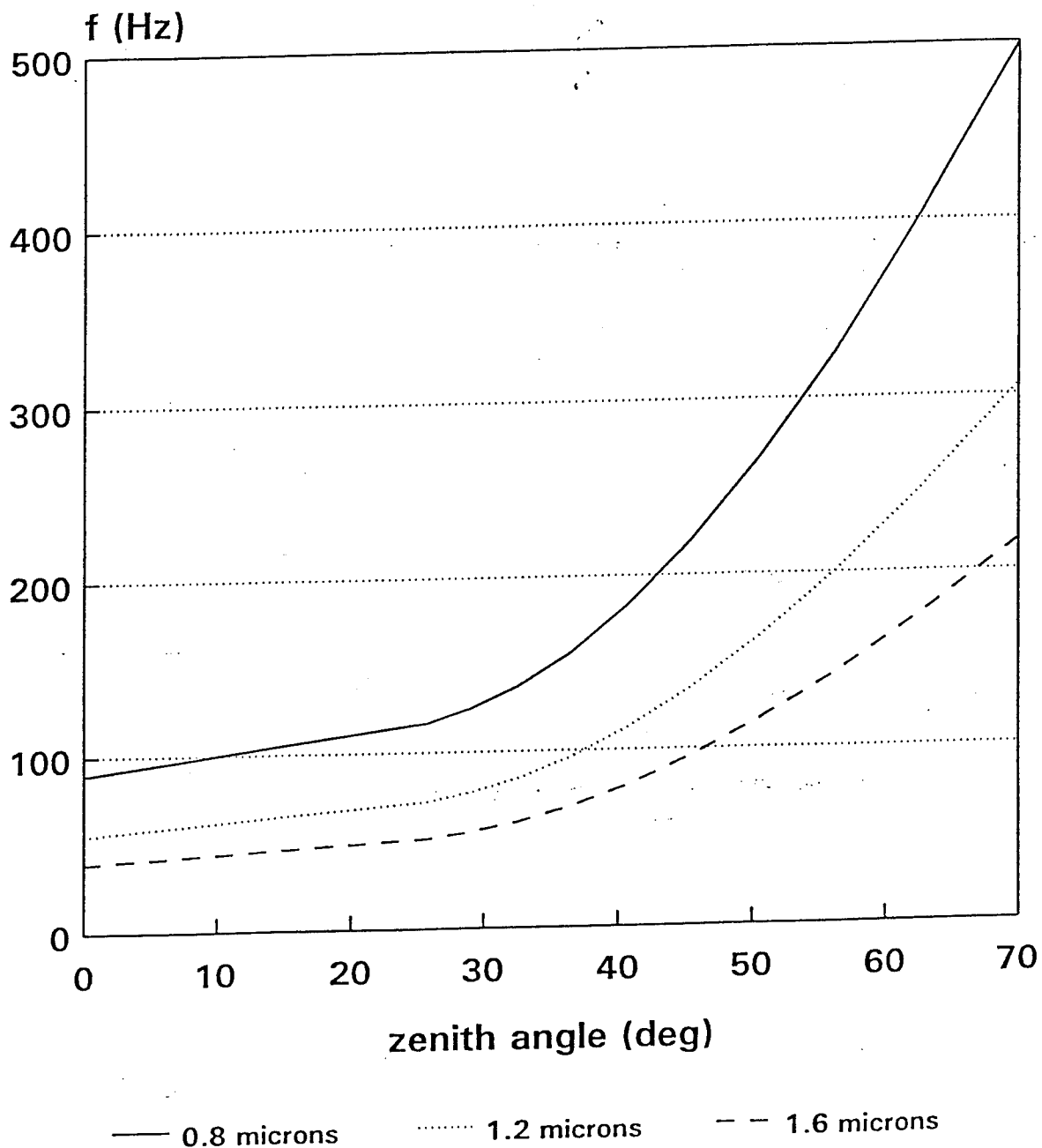# 1 deg/sec slew, Beland night model

f (Hz)

legend: —— 0.8 microns   ········ 1.2 microns   − − 1.6 microns

Figure 9: Greenwood frequency f_G vs. zenith angle for Beland night turbulence model at $\lambda = 0.8$, 1.2, and 1.6 μm.

3. <u>SIMULATIONS</u>

3.1. <u>SIMULATION DESCRIPTION</u>

The simulation used to compare adaptive optics configurations generates an ensemble of residual phase functions at the telescope pupil and calculates a sample-based mean optical transfer function (OTF) and an OTF variance. These results are used, with one exception, to generate all other outputs used in this study. The simulation has been validated extensively and is described thoroughly elsewhere [24].

User inputs include specifications which determine WFS subaperture and DM geometry in the pupil plane, photon flux at the WFS, and atmospheric seeing (r_o). The WFS and DM geometry are used with actuator DM functions to calculate the matrix H in the relation

$$\phi = \mathbf{H}\mathbf{v}, \tag{24}$$

where the elements of the vector ϕ are the x and y slopes at each WFS subaperture and the elements of $\mathbf{v}$ are applied DM voltages. Since (24) is in general an overdetermined system of equations, the inverse mapping $\mathbf{R}$ is determined from $\mathbf{H}$ using a least-squares method found in the IMSL library of numerical routines. Individual phase screen realizations are generated using Karhounen-Loeve routines [25] and the seeing specification. The photon flux at the WFS is used to calculate the wavefront measurement SNR.

For each imaging "frame" in the simulation ensemble, a realization of spatial turbulence is generated and written to an array representing the pupil plane of the telescope being simulated. Since the simulations for this work use a single phase screen located at the pupil plane to represent atmospheric turbulence, the imaging conditions allowing this approximation are assumed to exist [26]. This pupil phase function is then sampled using the locations of the WFS subapertures in the pupil; the gradient given by phase values at points bounding the subapertures is integrated numerically to produce a vector of x and y slopes. Random Gaussian noise is then added to the ϕ vector with a standard deviation calculated using [21]

$$\sigma = \frac{\pi d}{SNR \, r_o} \sqrt{\frac{\pi}{10}}, \tag{25}$$

where d is the length of one side of a subaperture, and SNR is the WFS signal-to-noise ratio calculated by

$$SNR = \frac{N}{\sqrt{N + 4\sigma_e^2}}, \tag{26}$$

where N is the number of photons collected by each subaperture per WFS integration time, σ_e^2 is the variance of the WFS detector read noise. The factor of $\sqrt{\pi/10}$ in (25) accounts for the averaging of noise fluctuations over 10 integration periods in a simple integrating servo loop, and the factor of 4 in (26) represents the number of pixels in the individual WFS slope sensors.

After measurement noise is added to ϕ, the DM voltage vector $\mathbf{v}$ is formed from the vector-matrix inner product $\mathbf{R}\phi$. The phase removed from the pupil phase map is likewise $-\mathbf{Hv}$, although the $\mathbf{H}$ matrix is not explicitly preserved to conserve memory. The pupil phase map then has some amount of uncorrected phase remaining, depending on the WFS noise and the WFS/DM geometry. The autocorrelation of the corrected phase map (the instantaneous AO-compensated OTF [26]) and its square are added to buffers to calculate the sample-based OTF moments described.

To account for finite bandwidth effects, the elements in the phase screen are shifted a small amount to mimic telescope tracking slew prior to subtraction of the phases in $-\mathbf{Hv}$. The magnitude of the shift is determined using the response time of the AO control loop and a relative wind velocity to account for tracking slew. A reasonable estimate for the relative wind observed by the WFS is the turbulence-weighted average velocity $\bar{v}$:

$$\bar{v} = \frac{\int_0^z v(\xi) \, C_n^2(\xi) \, d\xi}{\int_0^z C_n^2(\xi) \, d\xi}. \tag{27}$$

An approximate closed-form expression for the motion required of a single phase screen to simulate the effect of telescope slew can be written in terms of familiar quantities. This is done by calculating the turbulence-weighted average of the wind velocity raised to the 5/3 power:

$$\overline{v^{5/3}} = \frac{\int_0^z v^{5/3}(\xi)\, C_n^2(\xi)\, d\xi}{\int_0^z C_n^2(\xi)\, d\xi}. \tag{28}$$

Multiplying the numerator and denominator of (28) by constants and raising both sides to the 3/5 power gives

$$\left(\overline{v^{5/3}}\right)^{3/5} \approx \bar{v} = \frac{\left(\int_0^z v^{5/3}(\xi)\, C_n^2(\xi)\, d\xi\right)^{3/5}}{\left(\int_0^z C_n^2(\xi)\, d\xi\right)^{3/5}}, \tag{29}$$

which, using the definition [26] for r_o:

$$\frac{1}{r_o} = 5.4 \left(\frac{1}{\lambda^2} \int_0^z C_n^2(\xi)\, d\xi\right)^{3/5} \tag{30}$$

and the definition of Greenwood frequency (19), can be written

$$\bar{v} = \frac{f_G\, r_o}{0.43}. \tag{31}$$

Using $1/2\pi f_c$ as the control loop response time, the phase screen motion can then be written as

$$\bar{v}t \approx 2.32 \frac{f_G\, r_o}{2\pi f_c}. \tag{32}$$

Calculated $\bar{v}t$ results using (32) were compared to results obtained using the simulation and (5), the relation between Greenwood frequency and residual phase error due to finite bandwidth. For convenience, (5) is repeated here:

$$\sigma_{r,f_c}^2 = \left(\frac{f_G}{f_c}\right)^{5/3}.$$

First, the simulation was run with zero phase screen shift and zero WFS noise. By simulating an infinite control loop bandwidth and eliminating WFS noise, all sources of residual error except DM fitting error were removed. Then, the simulation was run with increasing amounts of phase screen shift. The squared error at zero shift was subtracted from the total error after each run, yielding a plot of residual error due to finite bandwidth vs. phase screen shift Δx. For a given Greenwood frequency, then, this plot of $\sigma_{r,f_c}^2(\Delta x)$ and (5) can be used to generate a plot of f_c vs. Δx. Finally, the inverse of the simulation $f_c(\Delta x)$

27

function was compared to (32) for correspondence using several AO geometries. Although an exact match was not expected, the reasonable correspondence (typically within a factor of 2) observed validates the derivation of $\bar{v}t$ given above.

3.2. SIMULATION MEASURES OF MERIT

Intelligent choices for measures of merit, or "metrics," are imperative when computer simulations are used to guide decision-making in any endeavor. For an adaptive optics study, the metrics chosen must correctly reflect changing AO performance as imaging wavelength, seeing, and reference brightness vary, as well as indicate potential improvements to be had from statistical processing of recorded image data.

Common imaging metrics that can give misleading results are the width at half-maximum of the average image of a point-like object (the PSF), and the Strehl ratio, S. For a pupil diameter $D \gg r_o$, with the width of the diffraction-limited OTF much larger than that of the OTF including aberrations, it can be shown that the average PSF consists of a diffraction-limited "core" surrounded by a diffuse "halo," as shown in Fig. 10. The relative amplitudes of the core and halo depend on the seeing and how well the AO system works, but it is clear that since the shape of the core depends primarily on diffraction, the width at half-maximum of the average PSF will be relatively insensitive to changes in AO performance. Similarly, while S is a sound metric for measuring AO performance at a single wavelength, it cannot be used alone to predict the optimum wavelength, since it simply increases monotonically to its asymptotic value of unity as λ is increased even though diffraction may cause the actual resolution to decrease, as discussed in the previous chapter.

The most easily calculated measure of merit is the average mean-square uncorrected phase error, or the "residual phase." This quantity is defined [21] as the integral over the pupil of the ensemble-average phase remaining after compensation:

$$\sigma^2 = \int W(\mathbf{r}) \; <\phi^2(\mathbf{r},t)> \; d^2\mathbf{r}, \tag{33}$$
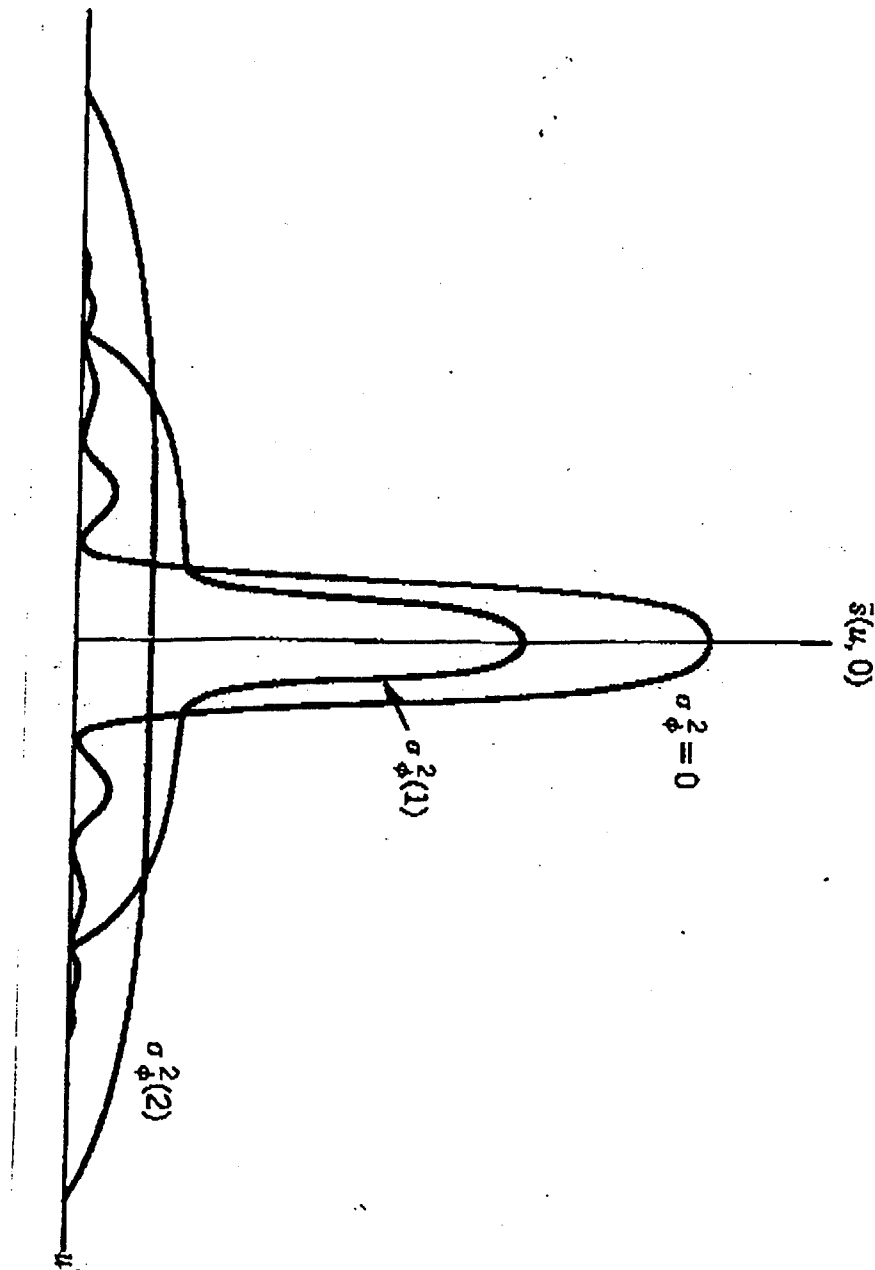
28

Figure 10: Diffraction-limited "core" and surrounding "halo" comprising the average point-spread function for three levels of residual phase variance in the pupil plane. From *Statistical Optics* by J.W. Goodman, John Wiley and Sons (1985). Reprinted by permission of John Wiley and Sons.

29

where W is the pupil weighting function in units of inverse area, $\mathbf{r}$ is the spatial coordinate vector in the x-y plane, ϕ is the instantaneous residual phase, and the $<>$ brackets indicate an ensemble average. Computationally, the simulation avoids summing the ensemble of $\phi(\mathbf{r},t)$ arrays in a buffer array by using the linearity of the integral and ensemble-average operator to change their order as shown:

$$\sigma^2 = < \int W(\mathbf{r})\phi^2(\mathbf{r},t)d^2\mathbf{r} > .\qquad (34)$$

In this manner, a single scalar is summed over all the frames instead of an array.

The mean-square residual phase is useful in determining the type of post-detection processing appropriate. As discussed by Nakajima and Haniff [27], a mean-square phase of less than four radians-squared allows the use of linear reconstruction techniques, which are preferred for speed and simplicity. Such methods are discussed further in this section. A larger error, conversely, dictates the use of nonlinear techniques such as Knox-Thompson or bispectrum phase-recovery algorithms. Such methods are collectively referred to as "speckle imaging" techniques and were developed to recover near-diffraction-limited images of relatively bright objects without the use of adaptive optics. As will be discussed in the next section, a preliminary decision on whether a given AO system's performance is sufficient in a given scenario may be made based on whether linear processing techniques will be effective as indicated by σ^2.

While the Strehl ratio approaches unity as λ is increased, σ^2 approaches zero. Thus neither S nor the mean-square residual phase may be used to compare AO system performance at different imaging wavelengths. The normalized on-axis intensity I_n used in the previous section is defined as the ratio of the energy at the center of the focal plane and the total intensity and can be used to compare systems at different λ. As previously discussed, this metric accounts for both PSF spreading from diffraction, which increases with λ, and the competing effect of spreading from residual aberration, which decreases with λ.

For any reasonable degree of compensation, the average point-spread function is small and has a steep derivative near the focal plane origin, so numerical integration of the PSF

to calculate I_n is likely to be inaccurate. Therefore, we make use of the average OTF as shown in the following relation

$$\frac{P(\mathbf{r} = 0)}{\int P(\mathbf{r})d^2\mathbf{r}} = \frac{\int H(\boldsymbol{\rho})d^2\boldsymbol{\rho}}{H(\boldsymbol{\rho} = 0)}, \tag{35}$$

where P is the average PSF, H is the average OTF, and $\boldsymbol{\rho}$ is the spatial frequency vector in the u-v plane. It is easy to show that the two numerators and denominators in (35) are Fourier transform pairs. Using (35), I_n can be calculated by integrating the average OTF normalized to be unity at zero spatial frequency.

The commonly-used Strehl ratio S is defined [17] as I_o/I_{dl}, where I_o is the observed on-axis intensity and I_{dl} is the on-axis intensity for a diffraction-limited optical system. A simple approximation to S is given by $exp(-\sigma^2)$, but the simulation calculates a diffraction-limited OTF by taking the autocorrelation of the aberration-free pupil function. Using the diffraction-limited OTF in (35) yields I_{dl}, which in turn gives S.

To properly calculate the integrals required for Strehl and I_n as wavelength changes, the radial extent of the OTF must be properly normalized. Put another way, the OTF expands or contracts in frequency space as λ changes, and this must be accounted for in numerical calculations. The easiest way to do this is to scale the size of individual pixels in the array holding the OTF by the inverse of λ, effectively changing $d\boldsymbol{\rho}$ in (35).

Since imaging wavelengths in the near-infrared through K-band were considered for different AO configurations, the camera noise characteristic of near-IR detectors is accounted for using a "noise-equivalent Strehl," S_{ne}. To calculate S_{ne}, the instantaneous AO-compensated OTF for each frame is Fourier-transformed to form the instantaneous PSF, which is then normalized to the correct signal photon count. Gaussian-amplitude white noise with variance characteristic of the imaging detector is then added to the instantaneous PSF. The resulting noisy distribution is transformed back to form a noise-corrupted instantaneous image spectrum and averaged as before to form an average OTF $H(\boldsymbol{\rho})$, which is then used with (35) and the diffraction-limited OTF to form S_{ne}.

The above measures of merit are referred to as "integrated metrics" and are most useful

for comparing performance of different systems or AO configurations; they provide little information concerning the linear resolution achievable with any particular system or configuration. However, the simplest estimate of linear resolution is found using S: Recall the well-known Rayleigh criterion for angular resolution θ is given by

$$\theta = 1.22\frac{\lambda}{D}, \tag{36}$$

where λ is the wavelength of the incident light and D is the diameter of an unobstructed circular aperture. Consider also that, as discussed in the previous chapter, the peak intensity P_o of an Airy point spread function is proportional to the square of the inverse of the angular resolution:

$$P_o \propto \left(\frac{D}{\lambda}\right)^2 \propto \frac{1}{\theta^2}. \tag{37}$$

If we infer that (37) holds approximately, with the same constant of proportionality, for a telescope with a central obscuration and some amount of uncorrected phase, then

$$\frac{\theta}{\theta_{ab}} = \sqrt{\frac{P_o}{P_{o,ab}}}, \tag{38}$$

where θ and P_o are given by (36) and (37) and θ_{ab} and $P_{o,ab}$ are the maximum angular resolution and peak intensity for the telescope with a secondary obscuration and residual atmospheric phase aberrations. An estimate for the achievable resolution θ_{ab} can then be given in terms of S and θ:

$$\theta_{ab} = \frac{\theta}{\sqrt{S}} = 1.22\frac{\lambda}{D\sqrt{S}}. \tag{39}$$

The linear resolution is then simply the product of θ_{ab} and the object range R. Comparison with (2) will show that θ_{ab} is inversely proportional to I_n.

Another linear resolution metric is the "cutoff" of the signal-to-noise (SNR) ratio of the estimated average OTF with AO compensation. The compensated OTF can be estimated by averaging an ensemble of star (point-source) images, and the cutoff is defined as the spatial frequency where the SNR of the OTF, averaged around the zero-frequency point to

reduce the spatial frequency to a single coordinate, decreases to unit value. The SNR of the OTF is calculated from the OTF moments described above using the definition

$$SNR(\rho) = \frac{<OTF(\rho)>}{\sqrt{<OTF(\rho)^2>}},\qquad(40)$$

where $\rho = |\boldsymbol{\rho}|$ is used as the argument to indicate the values are the average values at constant radius from zero. The significance of the SNR cutoff arises from the dependence of statistical post-processing methods, which will be used with the AO system in the AEOS design, on sample-based estimators for spectral moments such as the average and mean-square OTF. The SNR of an estimator is a direct indicator of how well the sample-based moment approximates the true moment formed by summing an infinite number of realizations.

Consider the average estimate $<\tilde{O}>$ of the object spectrum O formed using so-called pseudo-Weiner filter processing in combination with an AO system [11]:

$$<\tilde{O}(\boldsymbol{\rho})> = \frac{<I_i(\boldsymbol{\rho})> \tilde{H}^*(\boldsymbol{\rho})}{|\tilde{H}(\boldsymbol{\rho})|^2}\qquad(41)$$

where I_i is the spectrum of the ith instantaneous image in an ensemble, $\tilde{H}$ is the estimated average transfer function, and the * operator stands for complex conjugation. Using the spectral relation $<I_i(\boldsymbol{\rho})>= \tilde{H}(\boldsymbol{\rho})O(\boldsymbol{\rho})$, where $O(\boldsymbol{\rho})$ is the nonrandom object spectrum, (41) can be rewritten

$$<\tilde{O}> = \frac{<I_i> \tilde{H}^* O^* O}{<|I_i|^2>} = O\frac{|<I_i>|^2}{<|I_i|^2>},\qquad(42)$$

where the spatial frequency arguments are understood. Defining SNR_I as the mean over standard deviation of the ensemble-average image spectrum I and using the relation defining σ_I^2, the variance of I,

$$\sigma_I^2 = <|I|^2> -|<I>|^2\qquad(43)$$

in (42) allows one to write[†]

[†]B.L. Ellerbroek, personal communication

33

$$< \tilde{O} > = O \frac{| < I_i > |^2}{< |I_i|^2 >} = O \frac{SNR_I^2 \, \sigma_I^2}{\sigma_I^2 + SNR_I^2 \, \sigma_I^2} = O \frac{SNR_I^2}{1 + SNR_I^2} \qquad (44)$$

This result shows that at the spatial frequency where the image SNR = 1, the spectral components of the estimated object are half the value of the components of the object, O. Also, observe that (44) may be thought of as expressing an "estimation transfer function" $\tilde{O}/O$ in terms of SNR_I, which is directly related to the performance of the adaptive optics system. Starting again with (41) and rearranging slightly allows one to write the normalized square error in the estimation of O, expressing the previous result in a different way:

$$\frac{|O - < \tilde{O} >|^2}{|O|^2} = (\frac{1}{1 + SNR_I^2})^2 . \qquad (45)$$

Here, we see that at the frequency where the SNR = 1, the magnitude of the expected error in estimating the object spectrum is equal to half the the magnitude of the spectrum itself.

Finally, we can derive the SNR of the object spectrum estimate. Any $< \tilde{O} >$ formed using sample-based estimators as discussed above will vary as different data ensembles are used to form the estimators; that is, if, say, 200 image frames and 200 star-image frames were collected, two estimates of O could be formed using 100-frame ensembles from each of the two data sets to form $< I_i >$ and $\tilde{H}$ in (41). These two O estimates will differ according to $SNR_I(\rho)$. The two images formed from these estimated spectra will of course differ as well, with, in general, larger features varying relatively less than smaller features. If features corresponding to a certain spatial frequency vary substantially between images, those features can be considered noise and the effective resolution of the telescope-AO-processing combination has been reached. Calculation of SNR_O, the SNR of the object spectrum estimate, shows how randomness in estimated object spectra depends on SNR_I.

To calculate SNR_O, one must first write the variance of $\tilde{O}$. From (44), one may write the square of the mean estimate in terms of SNR_I as

$$|< \tilde{O} >|^2 = |O|^2 |\frac{SNR_I^2}{1 + SNR_I^2}|^2 . \qquad (46)$$

34

The mean of the squared estimate is formed by writing the instantaneous or unaveraged object spectrum estimate $\tilde{O}_i$ as follows [28]:

$$\tilde{O}_i = O \frac{< I_i > I_i}{< |I_i|^2 >} . \tag{47}$$

This allows one to write

$$< |\tilde{O}|^2 > = |O|^2 < |\frac{< I_i^* > I_i}{< |I_i|^2 >}| > = |O|^2 \frac{|< I_i >|^2 < |I_i|^2 >}{< |I_i|^2 >^2} = |O|^2 \frac{SNR_I^2}{1 + SNR_I^2} , \tag{48}$$

where I_i^* is the complex conjugate of the spectrum of the ith image in the ensemble and not to be confused with the on-axis intensity quantity used in the last section. The variance σ_O^2 is formed using the difference between (48) and (46):

$$\sigma_O^2 = < |\tilde{O}|^2 > - |< \tilde{O} >|^2 = |O|^2 \frac{SNR_I^2}{(1 + SNR_I^2)^2} , \tag{49}$$

and SNR_O is formed by taking the ratio of (41), the mean of $\tilde{O}$, and the square root of (49), yielding

$$SNR_O = \frac{O \frac{SNR_I^2}{1+SNR_I^2}}{\sqrt{|O|^2 \frac{SNR_I^2}{(1+SNR_I^2)^2}}} = SNR_I . \tag{50}$$

At the spatial frequency ρ where $SNR_I = 1$, then, $SNR_O = 1$ and the limiting resolution is reached in the estimate of the object spectrum and the resulting image. Since for a point source, $SNR_H = SNR_I$, the inverse of the SNR cutoff described above yields the limiting angular resolution of the AO-compensated telescope with post-processing. Also, the difference between (39) and the SNR cutoff gives the improvement in resolution due to post-processing.

Now, it is our experience that the SNR cutoff is somewhat insensitive to small changes in seeing or WFS signal. That is, when residual phase error due to these factors increases by a small amount, the frequency at which $SNR_I = 1$ may only decrease by a similar small amount, with a more pronounced change occurring in the SNR at midband frequencies. This

is shown for the case of a power spectrum SNR in Fig. 11.[‡] Further, certain actuator and subaperture pupil geometries, as well as small reductions in the imaging wavelength, may tend to boost the SNR of midband spatial frequencies at the expense of a small reduction in the SNR cutoff. To observe these changes quantitatively, we have used an SNR integral measure of merit (IMOM).

The IMOM is calculated by integrating the quantity SNR-1.0, averaged at constant radius about zero frequency from λ/r_o to the SNR cutoff. This corresponds to the shaded area in Fig. 12. The inner limit is chosen because we expect the SNR to be large at frequencies below λ/r_o (the "seeing spike") regardless of how well the adaptive optics work, so the low-frequency SNR values are not of interest. Similarly, we only integrate values of the SNR greater than unity because the values above unity are indicative of increased resolution due to adaptive optics. Using this metric, we can observe changes in midband resolution due to factors that only create a small change in the SNR cutoff.

_____

[‡]The SNR here was calculated using an ensemble of 100 frames, multiplying the SNR by 10 and changing the cutoff from the SNR = 1 frequency to SNR = 10.
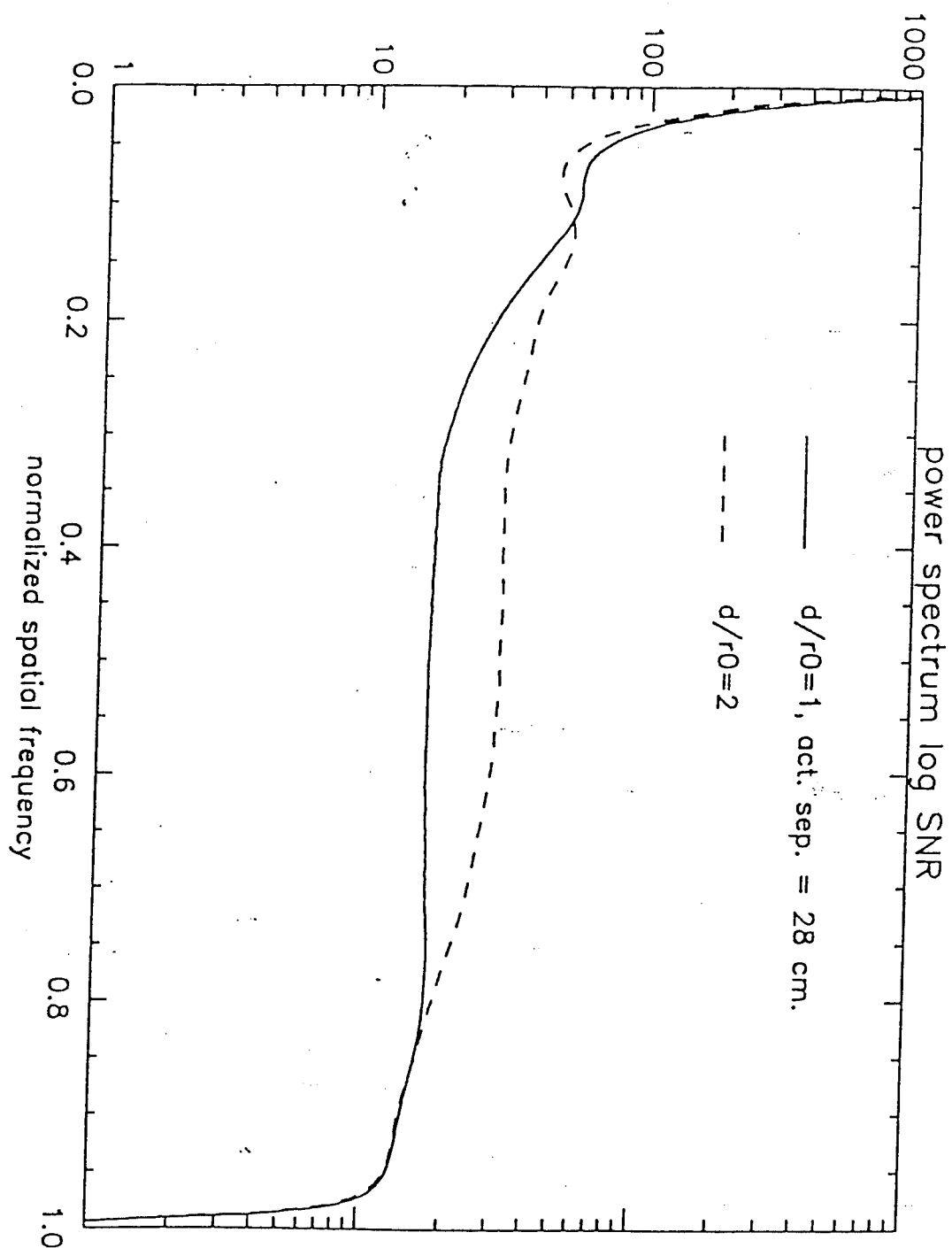
Figure 11: Power spectrum SNR for two different values of r_o. Note that although the SNR cutoffs (at an SNR of 10) are very similar, the midband behaviors are substantially different.
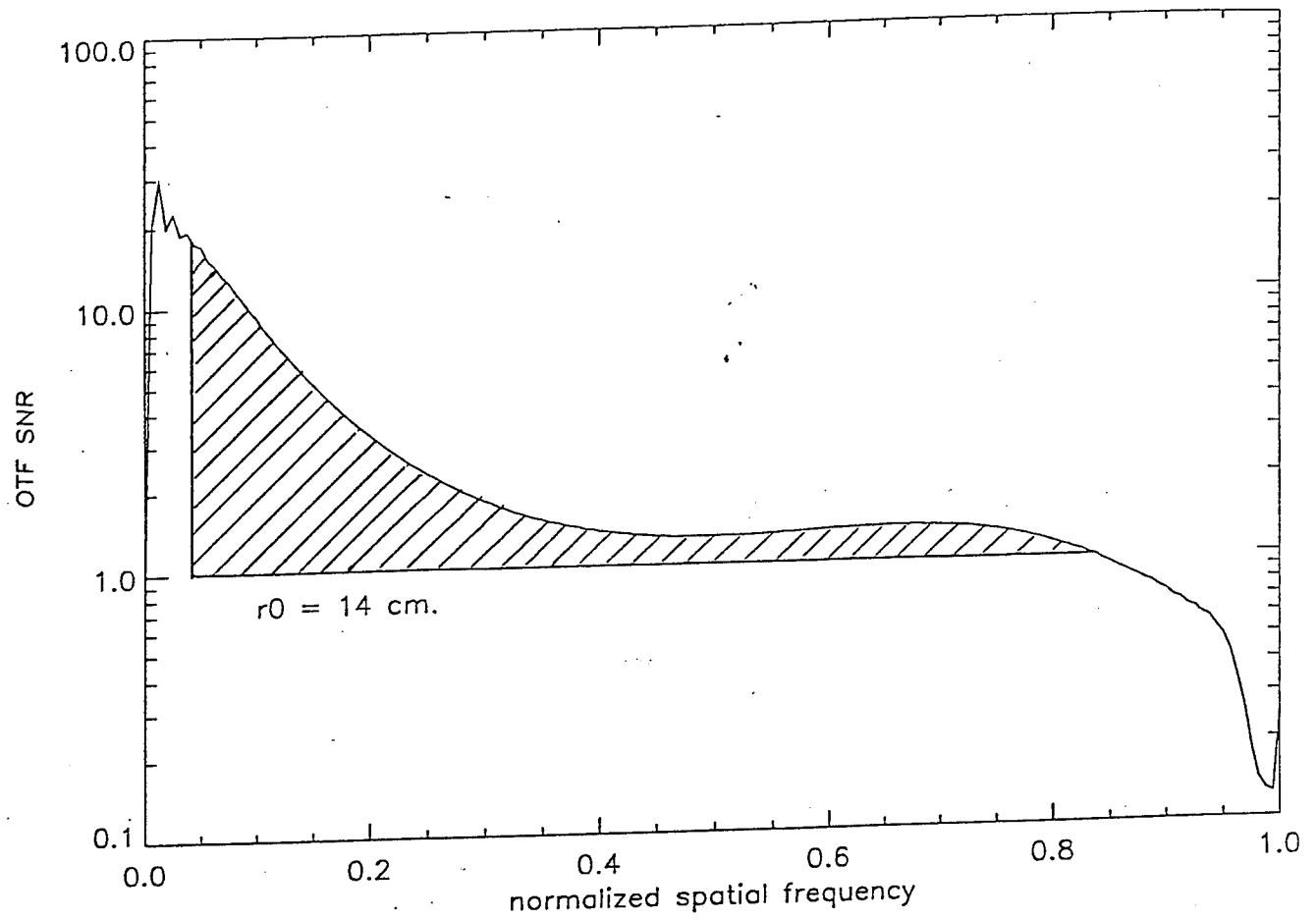
Figure 12: SNR for an average OTF showing the area integrated for the IMOM metric.

4. RESULTS AND DISCUSSION

4.1. SIMULATIONS

Four AO configurations were chosen for comparison with DM actuator spacings of 9, 12, 15, and 18 *cm*. With these spacings, the total numbers of actuators in the exposed pupil are 1200, 741, 505, and 325, respectively. The different systems will be referred to by the number of actuators; e.g. "the 1200 system" or "the 505 system."

The configurations were arrived at using preliminary work[††] assigned by the AEOS Scientific Advisory Board. While this work predicted the 741 system to be adequate, it did not show the system to be optimal in any sense, as we attempt to here. The additional systems, 1200, 505 and 325, were selected to incrementally span the space of actuator separations between 9 *cm* and 18 *cm*, the minimum and maximum spacings deemed practical given the requirement for a reasonably dim WFS reference and the seeing conditions at the AEOS site on Mt Haleakala.

Preliminary calculations eliminated the 1200 system from consideration due to WFS noise. The photon flux given by the visual magnitude 6 target in our scenario would yield approximately 10 PDEs per subaperture per sampling period for the 1200 system running at a closed-loop bandwidth of 300 Hz, depending on WFS quantum efficiency. Since our comparison scenario specifies a fairly high Greenwood frequency, lower bandwidths would result in substantially increased residual error while still not increasing the number of PDEs to even 50. Using a wave-optics simulation of a Hartmann wavefront sensor [29,30], this signal level was shown to produce unusably noisy wavefront measurements, so the full 1200 system was not simulated.

————

[††]The original AEOS design work was accomplished by M.C. Roggemann, B.L. Ellerbroek, D.W. Tyler, and M. Von Bokern of the USAF Phillips Laboratory, and T. Gray of W.J. Schafer Associates. While this work was briefed to the SAB, it was not documented in a report.

Also, simulations to validate (12) using the 70-degree zenith conditions revealed that, while the 741 and 505 systems yielded similar resolutions at their respective optimal wavelengths as measured by I^*, the 325 system resolution at its λ_o was only three-fourths that of the 741 system. Although finite bandwidth effects and WFS noise were not included in these runs, and these effects could possibly have impacted the 741 and 505 systems more severely than the 325, the lowest-order system was dropped from consideration as well. After including bandwidth and WFS noise in simulations of the remaining systems, the initial 325 system results were compared with the new 741 and 505 results to see if further study was required.

Next, optimum closed-loop bandwidths for the remaining systems, 741 and 505, were calculated using (16), which has very good correspondence with simulation results. For the 70-degree scenario, these bandwidths were $f_{co} = 300$ and 400 Hz, respectively. These bandwidths, in combination with the calculated photon flux from the WFS reference at visual magnitude 6, were used to calculate a λ_o for the systems with finite bandwidth and WFS noise effects included. Both the 741 and 505 systems had a peak I^* very near to 1.6 μm, the near-infrared H band. Note for purposes of simulating the individual systems, the atmospheric transmission window nearest λ_o is used for the imaging wavelength rather than λ_o.

The results from the simulations with $\lambda = 1.6$ μm are shown in Table 2. Note that while the normalized on-axis intensity, Strehl, and mean-square residual phase σ^2 are marginally higher for the 741 system, the SNR cutoff and integral measure of merit (IMOM) are somewhat higher for the 505 system. This can be understood by considering that while I^*, S, and σ^2 involve the first moment of the instantaneous OTF, the SNR cutoff and IMOM include the *variance* of the OTF. This implies that the 741 system single-frame results are more broadly scattered about their respective mean values than the corresponding 505 results. We attribute this result to lower WFS noise in the larger subapertures of the 505 system and the reduced susceptibility to bandwidth errors in the smaller system [16]. Note that with an r_o of 17.2 cm at H band, the 505 system still provides adequate spatial sampling of

the wavefront with subapertures approximately 15 *cm* in diameter.

Another way to view this phenomenon is to recall that the wavefront reconstructor used in both systems is a least-squares estimator; that is, the reconstructor treats all WFS measurements as equally valid and fits the DM voltages to the WFS signals in a least-squares sense. If the WFS measurements are noisy, then that noise is observed in the DM voltages, as well. The 741 system simulations show a higher variance simply because the larger number of WFS measurements lead to more noise in the DM voltages.

In terms of the effect on linear post-processing, consider the simple deconvolution scheme

$$\tilde{O}(\boldsymbol{\rho}) \; = \; \frac{< I(\boldsymbol{\rho}) >}{\tilde{H}(\boldsymbol{\rho})}, \tag{51}$$

where the above quantities are defined consistently with the previous section. For the 741 system, higher I_n and Strehl and lower mean-square residual phase mean less numerical noise in the division used for (51) because the sharper ensemble-average point-spread function manifests itself as a relatively broader average OTF estimate, $\tilde{H}$. However, for the pseudo-Wiener filter given in (41), the resolution limit in the object estimate after processing is given by the SNR cutoff. Also, the lower SNR cutoff for the 741 system means the resolution limit in estimated objects will vary between data sets slightly more than with the 505 system, all other conditions being equal.

Recent work on *miminum-variance reconstructors* [24,31] has shown that these algorithms, while somewhat more difficult to implement, provide a significant increase in low-light-level performance. Such algorithms, by receiving feedback from observations of the DM figure, estimate the SNR of WFS measurements and adjust actuator voltages accordingly. In the limit of extremely low WFS SNR, the minimum-variance reconstructor will drive the DM flat due to lack of reliable data; the least-squares reconstructor will use the noisy WFS data and can actually increase image blur beyond that observed with no compensation at all.

Further, extensions of speckle holography [28,32] to AO systems have shown that accumulated wavefront sensor data can be used to partially compensate for finite-bandwidth

residual phase errors [33]. One implication of this work is that the closed-loop bandwidth can be reduced below the f_{co} given by (16) to decrease sensor noise with the resulting temporal errors compensated for in post-processing. The result would be a net increase in the SNR cutoff for any system, since finite-bandwidth residual phase would remain the same and WFS noise would be reduced.

Now, as previously discussed, imaging detectors in the 1-5 μm band are at best 10 times noisier than silicon detectors in the 0.4-1 μm band, a fact of considerable significance for satellite imaging, where blur due to object motion limits the total observation time. As an example, calculations for the WFS yield a PDE rate of 1.6×10^7 per second in the AEOS telescope pupil at a wavelength of .65 μm for an object magnitude of 5.9, telescope transmission to the camera of 0.5, and a detector quantum efficiency of 0.8. Assuming the reflected spectrum approximately matches a blackbody at 5900 K, the blackbody photon curve shown in Fig. 13 can be used to calculate a PDE rate of about 2×10^7 per second at $\lambda = 0.8$ μm and 1×10^7 per second for $\lambda = 1.6$ μm. Now, since the maximum exposure time [34] for the imaging camera goes as λ, the total number of photons per camera is about the same for both wavelengths; that is, there are twice as many photons incident per second at 0.8 μm, but the maximum exposure time is half that allowed at 1.6 μm. If we consider a silicon CCD with 10 noise electrons per pixel and a 128 $\times$ 128-pixel detector array, the square root of the noise variance is

$$\sqrt{p\sigma_e^2} = \sqrt{16384 \times 100} = 1280, \tag{52}$$

where p is the number of exposed pixels and σ_e^2 is the detector noise variance per pixel.

For imaging at 1.6 μm, the maximum spatial resolution will be half that at 0.8 μm, so only one-fourth of the 16384 pixels used previously will be required at the longer wavelength. With σ_e ten times the figure used for silicon, $\sqrt{p\sigma_e^2} = 6400$, or 5 times 1280. This means regardless of exposure time, the detector SNR will be approximately five times lower at 1.6 μm than at 0.8 since the two mean PDE counts are the same. The maximum exposure time t_o can be calculated [34] in terms of the satellite's apparent rotation ω and angular subtense
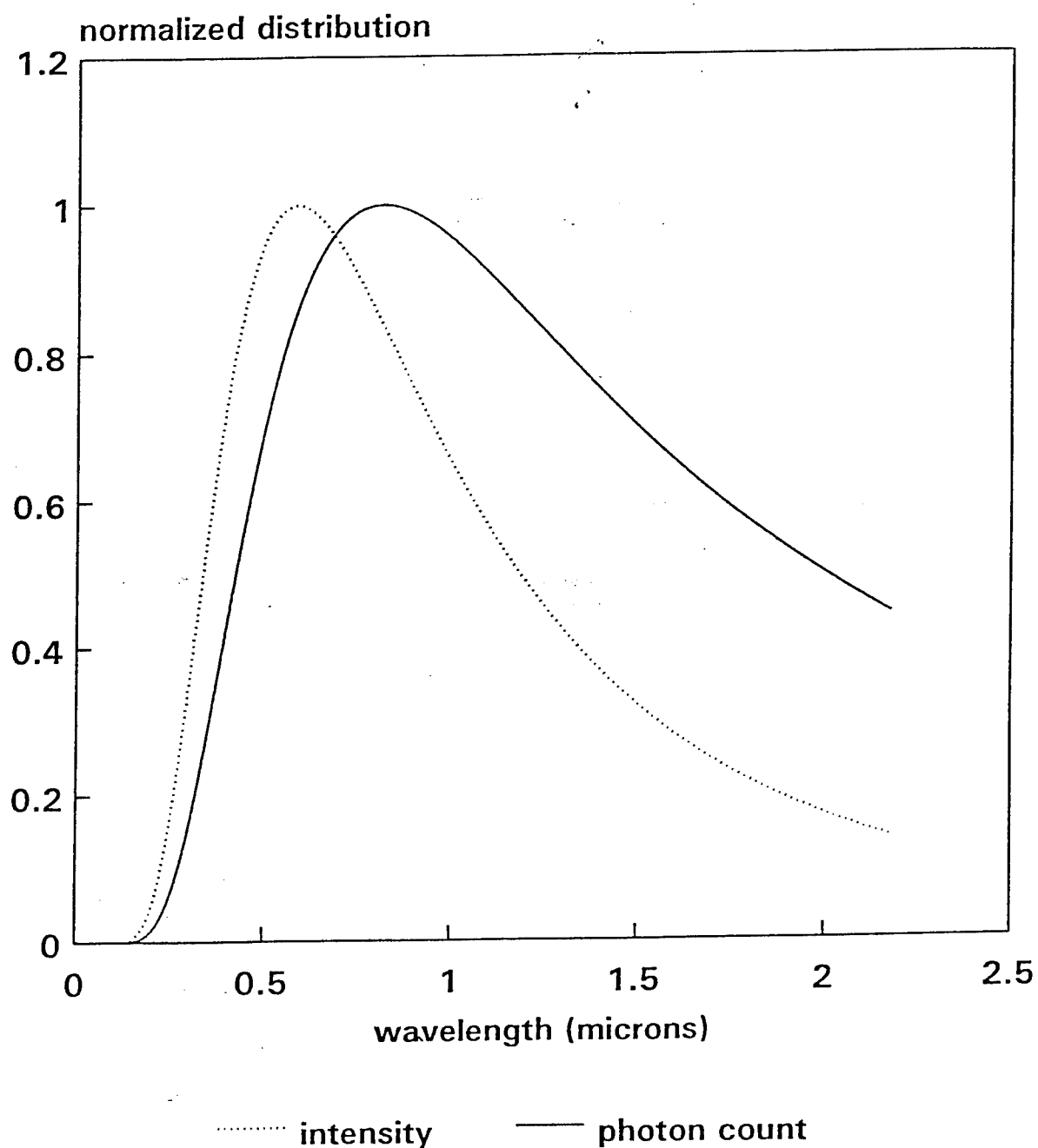
blackbody and photon distributions

Figure 13: Blackbody intensity and photon density distributions for a 5900 K source.

L, the telescope's maximum resolution $\Omega = 1.22\lambda/D$, and the desired resolution ρ given normalized to Ω:

$$t_o = \frac{\Omega}{\omega L \rho}. \qquad (53)$$

For the case above, where the object $m_v = 5.9$ at 70 degrees zenith, we can assume a 10 m object at the 1200-km range specified earlier. With an approximate orbital velocity of 7 km/sec, t_o is about 9 seconds at 1.6 μm and 4.5 seconds at 0.8 μm. Now, to calculate an estimator for the average image spectrum and average OTF for any of the deconvolution schemes discussed, an ensemble of short-exposure images is desirable so residual (post-AO) tilt can be removed by centroiding algorithms, maximizing resolution [11]. If 200 frames are desired and the imaging camera readout efficiency is such that 90 percent of each camera cycle is spent on exposure and 10 percent reading out, the signal photons collected per frame is $9 \times 1 \times 10^7 \times .9 \times .005 = 4 \times 10^5$ for a per-frame SNR of about 63 for $\lambda = 1.6$ μm, as compared to 316 for 0.8 μm. The individual exposures for this example are about 41 $msec$ long.

To examine the effect this difference in camera signal-to-noise can have on resolution, consider another simulation for which we have both an average OTF and the necessary OTF SNR as a function of normalized spatial frequency ρ. Here, the object m_v is 5, or about 2.5 times brighter than the $m_v = 5.9$ object considered previously. The number of PDEs per second at $\lambda = 0.8$ μm is approximately 45×10^6, yielding a per-frame count of about 4×10^5 for an ensemble of 100 frames and $t_o = 1$ s; this yields the same camera SNRs as the previous example, for which an OTF was not produced as output. The reduced t_o was chosen arbitrarily, but could be calculated by reducing the range from 1200 to 600 km, increasing both ω and L. The OTF for this case, normalized to unit value at $\rho = 0$, is shown in Fig. 14.

Equating the denominators from (35) shows that the OTF at zero frequency is equal to the total number of PDEs per frame. The camera SNR effect can be observed by considering a point near the OTF SNR cutoff, say 0.8. Here, the mean OTF is $0.02 \times 4 \times 10^5 = 8000$.
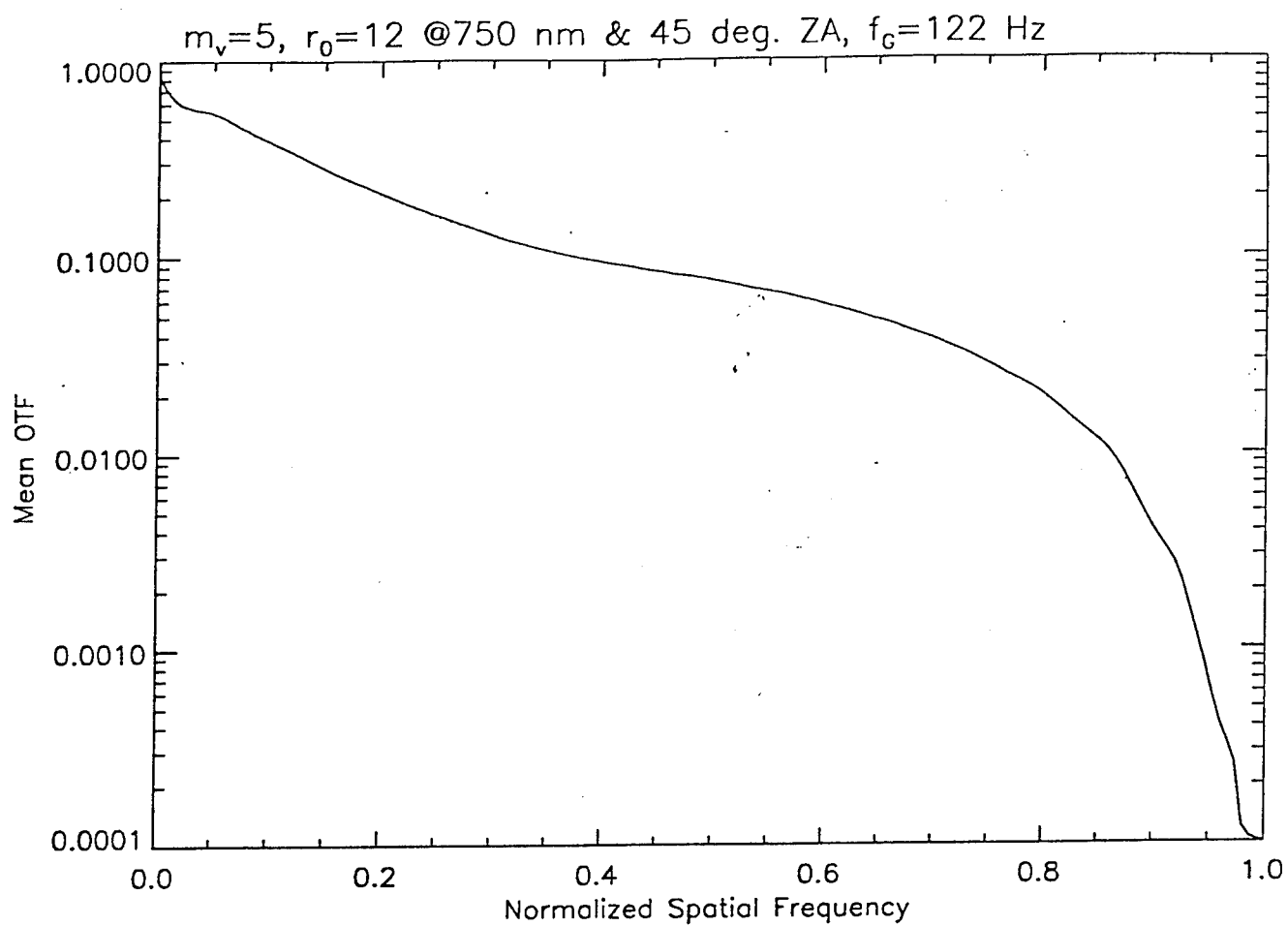
44

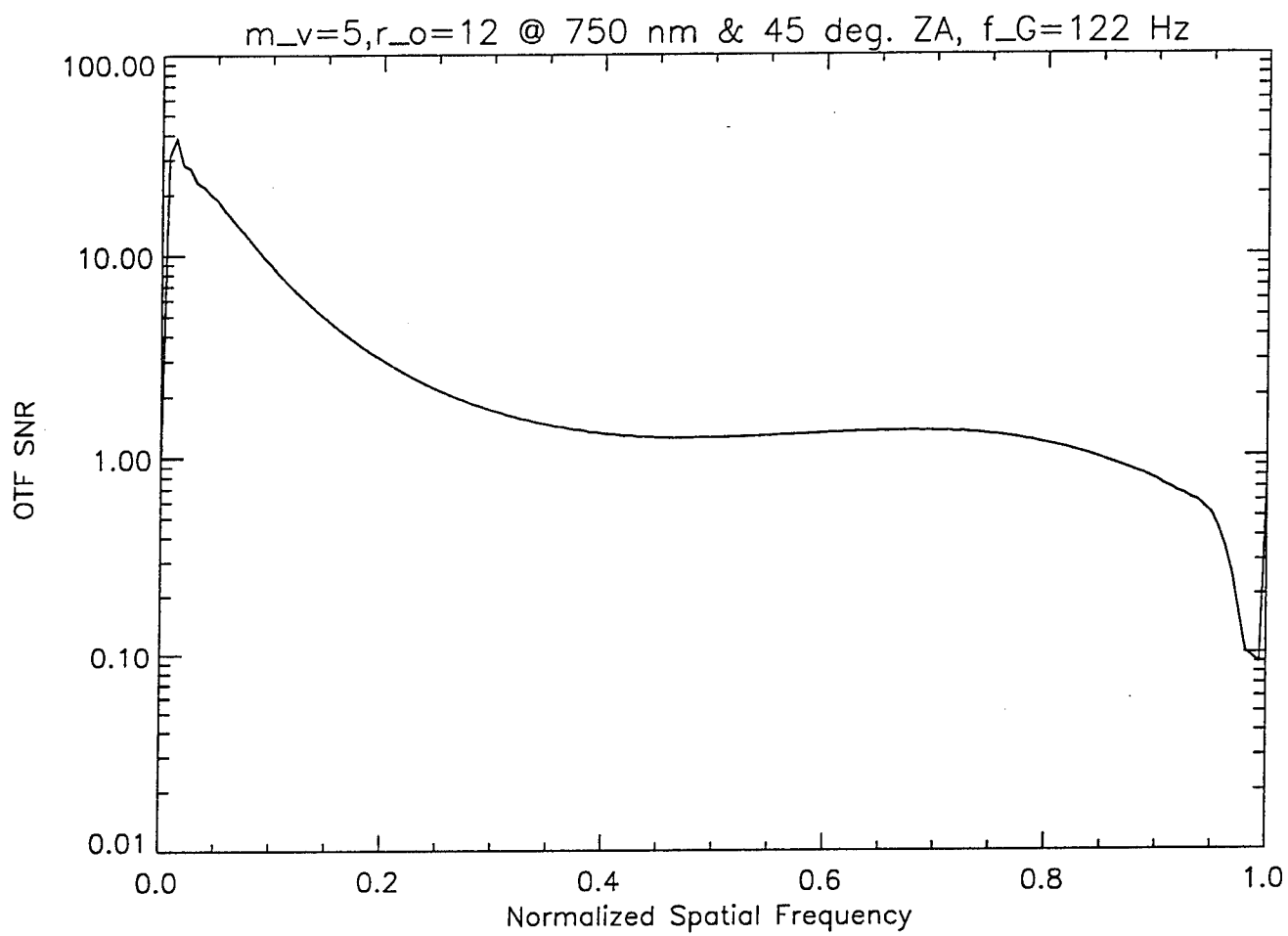Figure 14: Average OTF used to calculate camera noise effects.

Figure 15: SNR of the average OTF shown in Fig. 14.

From the OTF SNR shown in Fig. 15 and (40), this yields an OTF standard deviation σ = 8000/1.14 = 7017. Since the additive noise from the camera is independent of the atmospheric random process and is reasonably approximated by Gaussian white noise, the camera variance is independent of spatial frequency and can be simply added to the atmospheric variance at $\rho = 0.8$. Using the result from (52), this gives a σ corrected for camera noise = $\sqrt{7017^2 + 1280^2}$ = 7133 and a new OTF $SNR|_{\rho=0.8}$ of 1.12 for a silicon detector. For the longer wavelength detector, the new variance is $\sigma = 9497$, yielding an $SNR|_{\rho=0.8} = 0.84$. At lower spatial frequencies, of course, the effect of camera noise is not nearly as pronounced, but this example shows that detector characteristics can strongly affect the resolution of an image even with reasonably high camera signal-to-noise.

For $\lambda = 0.8$ μm, r_o is only 7.5 cm at 70 degrees zenith. For the first simulations at 0.8 μm, then, the zenith angle was reduced to 45 degrees so spatial sampling requirements can be met with the 505 system. Using the techniques used to calculate the photon flux at a zenith angle of 70, we arrive at an object visual magnitude of 4.3 at 45 degrees zenith, over 5 times brighter. From Table 3, the 741 system again performs better in terms of S, I_n, and residual phase error. With the WFS noise somewhat reduced, the marginal performance over the 505 system is increased substantially; however, the SNR cutoff and IMOM are still slightly lower for the 741 system. Again, the marginal performance indicates the 741 system is less affected by WFS noise than at 70 degrees zenith.

Finally, we compare the systems at $\lambda = 0.8$ μm and 70 degrees zenith angle. Here, the drastically reduced seeing conditions noted above caused the 505 system to fail completely due to lack of adequate spatial sampling [35]. In this situation, the undersampling of the 505 wavefront sensor causes the reconstructor to alias power into low spatial frequencies with the result that, similar to a case with extremely low WFS SNR, the AO system actually decreases image quality. The 741 system, however, retains a mean-square residual phase error of just over 4 radians-squared and an SNR cutoff of 0.25. As we have discussed, this residual phase is at the upper limit of the error allowed if linear post-processing techniques are to be used. Comparing the SNR cutoff of one-fourth of the diffraction limit to the

limit with no compensation, approximately 0.02, the AO system combined with linear post-processing would yield a more than ten-fold improvement. This SNR cutoff also compares reasonable well with the SNR cutoff of the 505 system at 1.6 μm; since the figure of 0.945 for the 505 system is normalized to the diffraction limit at twice the wavelength, the 741 system cutoff at 0.8 μm is over half the cutoff of the 505 system operating at its optimal wavelength. Although an average OTF was not produced for this case, accounting for camera noise effects would reduce this difference further.

4.2. <u>SYSTEM SELECTION AND ABSOLUTE PERFORMANCE</u>

From the results described in the last section, the 741 and 505 systems perform similarly, with the 741 system being somewhat more robust at imaging wavelengths < 1μm. However, the fact that the 741 system continues to perform adequately at even 70 degrees zenith angle, where spatial undersampling drives the 505 system to actually increase error, is an important consideration for satellite imaging directed by the military. For this application, the timeliness of delivered data can be critical, and as we have shown, the probability of a satellite passing the observatory increases with zenith angle. This leads us to recommend the AEOS adaptive optics use a configuration with about 741 DM actuators. Of course, differences in design, control, and fabrication techniques may cause the ultimate design to differ from this figure, but we anticipate the AEOS AO system will be similar to the 741 system described here. With the Beland atmospheric data for the AMOS site as a guide, we also recommend the AO system be designed to have a maximum closed-loop bandwidth of at least 400 Hz.

Other considerations weighing in favor of the 741 system include the development of minimum-variance wavefront reconstruction techniques and the use of speckle-holography processing in combination with AO. These techniques will increase the OTF SNR and IMOM of the 741 system. Also, current plans call for future installation of a laser guidestar system at the AEOS site; developments at the SOR have shown that the ability to point the laser

guidestar can reduce residual phase errors due to AO loop bandwidth, again increasing the OTF SNR and IMOM. Rayleigh-backscatter guidestars used to sense high-order turbulence modes can also decrease WFS measurement noise relative to a dim object.

Finally, we present example estimates of the linear resolution possible with the 741 system at 45 degrees zenith at 0.8 μm and 70 degrees zenith at 1.6 μm. Recall the seeing and Greenwood frequencies for the two scenarios are 11.6 cm and 122 Hz for the 45 degree case and 17.2 cm and 217 Hz for the 70 degree case.

To estimate the linear resolution limit before processing, we use the Strehl angle given in (39). For $\lambda = 0.8$ μm, the diffraction-limited angular resolution is reasonably approximated by 1.22 $\lambda/D \approx 2.66$ $\times 10^{-7}$. At a distance of 1000 km, for example, this translates to about 27.5 cm of linear resolution. Dividing by $1/\sqrt{S}$ with a Strehl of 0.54 gives about 1.4 times the diffraction limit or 37.5 cm. With post-processing, the linear resolution limit can be estimated by multiplying the diffraction-limited resolution by the inverse of the SNR cutoff, giving $27.5/0.925 \approx 30$ cm for the 45 degree, $\lambda = 0.8$ μm case.

For the 70 degrees zenith scenario, $\lambda_o = 1.6$ μm, and the diffraction-limited linear resolution at our example range of 1000 km is about twice the previous limit or about 55 cm. Using the Strehl of 0.38 as before yields a resolution without post-processing of about 89 cm. The SNR cutoff of 0.85 gives resolution with processing of about 65 cm.

5. <u>CONCLUSIONS</u>

We have developed an algorithm to guide the use of computer simulations in the design of application-specific adaptive optics (AO) systems. We used this method to specify the number of deformable-mirror actuators and closed-loop bandwidth for the Advanced Electro-Optical System (AEOS) telescope AO system. To develop the algorithm, we presented analysis to show the normalized on-axis intensity can be minimized for a given AO configuration by selecting an optimum imaging wavelength. This wavelength, λ_o, minimizes the combined effects of diffraction (which increases with wavelength) and residual phase aberration (which decreases as wavelength increases). We also showed that the closed-loop AO bandwidth minimizing the sum of wavefront sensor noise error and control loop lag error is independent of wavelength. This allowed the optimum bandwidth-wavelength combination for each AO configuration to be calculated non-iteratively in two steps. We described a high-fidelity computer simulation and measures of merit used to select from among four candidate configurations. Finally, we presented simulation results used to select the AEOS adaptive optics configuration; we recommend the AEOS system use approximately 700 actuators with a maximum closed-loop bandwidth of at least 400 Hz.

REFERENCES

[1] J.W. Hardy, "Active optics: A new technology for the control of light," *Proc. IEEE* **66** (1978)

[2] D. Greenwood and C. Primmerman, "Adaptive optics research at Lincoln Laboratory," *MIT Lincoln Laboratory Journal* **5** (1992)

[3] R.K. Tyson, "Wavefront correction," in *Principles of Adaptive Optics*, pp. 185-210, Academic Press, Boston (1991)

[4] F. Roddier, "Astronomical adaptive optics with natural reference stars," *Proc. Laser Guide Star Adaptive Optics Workshop, Vol. 1*, Albuquerque, New Mexico (1992)

[5] G. Rousset, *et al.*, "Adaptive optics prototype system for infrared astronomy," *Proc. SPIE* **1237** (1990)

[6] K.E. Kissell, J.V. Lambert, J. Africano, "Determination of thermally-induced bending of spacecraft booms by exploitation of adaptive optics images: the HST solar arrays," *OSA Conference on Adaptive Optics for Large Telescopes*, Lahaina, Maui, Hawaii (1992)

[7] J. Albetski, "History of the AMOS 1.6 meter telescope compensated imaging system," *OSA Conference on Adaptive Optics for Large Telescopes*, Lahaina, Maui, Hawaii (1992)

[8] R.Q. Fugate *et al.*, "Two generations of high-bandwidth laser guide star adaptive optics at the SOR," *Proc. Laser Guide Star Adaptive Optics Workshop, Vol. 1*, Albuquerque, New Mexico (1992)

[9] R.Q. Fugate, *et al.*, "Measurement of atmospheric wavefront distortion using scattered light from a laser guide star," *Nature* **353** (1991)

[10] M.C. Roggemann, "Limited degree-of-freedom adaptive optics and image reconstruction," *Applied Optics* **30** (1991)

[11] M.C. Roggemann, D.W. Tyler, M.F. Bilmont, "Linear reconstruction of compensated

images: theory and experimental results," *Appl. Optics* **31**, (1992)

[12] M.F. Bilmont, *et al.*, "Effects of predetection atmospheric compensation and post-detection image processing on imagery collected at a ground-based telescope," *Proc. SPIE* **1688** (1992)

[13] M.C. Roggemann *et al.*, "Compensated speckle imaging: theory and experimental results," *OSA Conference on Adaptive Optics for Large Telescopes*, Lahaina, Maui, Hawaii (1992)

[14] B.L. Ellerbroek, "Demonstration of improved resolution by deconvolution of laser guide star compensated images," *Proc. Laser Guide Star Adaptive Optics Workshop, Vol. 1*, Albuquerque, New Mexico (1992)

[15] N.A. Miller, J.S. Fender, and D.W. Tyler, "A methodology for adaptive optics design for the Advanced Electro-Optic System (AEOS)," *Proc. ICO Congress 16 Conference on Active and Adaptive Optics* (1993)

[16] F. Roddier, *et al.*, "One-dimensional spectra of turbulence-induced Zernike aberrations: time-delay and anisoplanicity error in partial adaptive optics compensation," *JOSA A* **10** (1993)

[17] M. Born and E. Wolf, "The diffraction theory of abberrations," in *Principles of Optics* 6 ed., Pergemon Press, Sydney (1989)

[18] G. Rousset, *et al.*, "Adaptive optics prototype system for infrared astronomy," *Proc. SPIE* **1237** (1990)

[19] R.J. Noll, "Zernike polynomials and atmospheric turbulence," *J. Opt. Soc. Am.* **66** (1976)

[20] D.P. Greenwood, "Bandwidth specification for adaptive optics systems," *J. Opt. Soc. Am* **67** (1977)

[21] B. Welsh and C. Gardner, "Performance analysis of adaptive-optics systems using laser guide stars and slope sensors," *JOSA A* **6** (1989)

[22] D. Fried, "Anisoplanitism in adaptive optics," *J. Opt. Soc. Am.* **72** (1982)

[23] R.R. Beland, J.H. Brown, R.E. Good, E.A. Murphy, "Optical turbulence characterization of AMOS, 1985," AFGL-TR-88-0153, Air Force Geophysics Laboratory, Hanscomb AFB, Mass. (1989)

[24] M.C. Roggemann, "Optical performance of fully and partially compensated adaptive optics systems using least-squares and minimum-variance phase reconstructors," *Comp. Elect. Engr.* **18** (1992)

[25] G. Cochran, "Phase screen generation," tOSC TR-663, the Optical Sciences Corporation, Placentia, California (1985)

[26] J. Goodman, "Imaging through randomly inhomogeneous media," in *Statistical Optics*, John Wiley and Sons, New York (1985)

[27] T. Nakajima and C.A. Haniff, "Partial adaptive compensation and passive interferometry with large ground-based telescopes," *Pub. Astr. Soc. Pacific* **105** (1993)

[28] J. Primot, G. Rousset, and J.C. Fontanella, "Deconvolution from wavefront sensing: a new technique for compensating turbulence-degraded images," *J. Opt. Soc. Am A* **7** (1990)

[29] D.W. Tyler and G.C. Loos, "Simulation study of a low light-level wavefront sensor driving a low-order, near-IR adaptive optics system," *Proc. IAU Conf. 158 on Very High Angular Resolution Imaging*, Sydney (1993)

[30] D.W. Tyler, G. Rousset, S.R. Restaino and G.C. Loos, "Low light-level adaptive optics for a two-telescope interferometer scheme," *Proc. SPIE* **2029** (1993)

[31] B.L. Ellerbroek, "First-order performance evaluation of adaptive optics systems for

atmospheric turbulence compensation in extended-field-of-view telescopes," *J. Opt. Soc. Am. A* **11** (1994)

[32] J.D. Gonglewski, *et al.*, "First astronomical application of post-detection turbulence compensation: Images of α Aurigae, ν Ursa Majoris, and α Geminorum using self-referenced speckle holography," *Appl. Opt.* **29** (1990)

[33] M.C. Roggemann and J.A. Meinhardt, "Image reconstruction by means of wavefront measurements in closed-loop adaptive optics," *J. Opt. Soc. Am. A* **10** (1993)

[34] P.D. Shubert, "Satellite imaging with speckle interferometry," *Proc. SPIE* **1351** (1989)

[35] D.W. Tyler and M.C. Roggemann, "The effect of wavefront undersampling on signal-to-noise ratio in adaptive optics systems," *Proc. SPIE* **1688** (1992)

TABLES

TABLE I.

Zenith angle	Engagements
70	0.45
45	0.20
20	0.07

Table 1: Percentage of total observatory passes available as imaging engagements as a function of zenith angle.

TABLE II.

	741 acuators	505 actuators
σ_r^2	1.21	1.93
I_n	0.224	0.21
S	0.54	0.50
SNR_{cutoff}	0.925	0.923
IMOM	2.94	3.28

Table 2: Comparison metrics for $\lambda = 1.6 \ \mu m$, zenith angle = 70.

TABLE III.

	741 acuators	505 actuators
σ_r^2	1.78	3.12
I_n	0.31	0.28
S	0.38	0.34
SNR_{cutoff}	0.85	0.89
IMOM	1.6	1.75

Table 3: Comparison metrics for $\lambda = 0.8 \ \mu m$, zenith angle = 45.